Sparse Reconstruction of Compressive Sensing Magnetic Resonance Imagery Using a Cross Domain Stochastic Fully Connected Conditional Random Field Framework

by

Yaguang Li

A thesis
presented to the University of Waterloo
in fulfillment of the
thesis requirement for the degree of
Master of Applied Science
in
Systems Design Engineering

Waterloo, Ontario, Canada, 2016

I hereby declare that I am the sole author of this thesis. This is a true copy of the thesis, including any required final revisions, as accepted by my examiners.

I understand that my thesis may be made electronically available to the public.

Abstract

Prostate cancer is a major health care concern in our society. Early detection of prostate cancer is crucial in the successful treatment of the disease. Many current methods used in detecting prostate cancer can either be inconsistent or invasive and discomforting to the patient. Magenetic resonance imaging (MRI) has demonstrated its ability as a non-invasive and non-ionizing medical imaging modality with a lengthy acquisition time that can be used for the early diagnosis of cancer. Speeding up the MRI acquisition process can greatly increase the number of early detections for prostate cancer diagnosis.

Compressive sensing has exhibited the ability to reduce the imaging time for MRI by sampling a sparse yet sufficient set of measurements. Compressive sensing strategies are usually accompanied by strong reconstruction algorithms. This work presents a comprehensive framework for a cross-domain stochastically fully connected conditional random field (CD-SFCRF) reconstruction approach to facilitate compressive sensing MRI. This approach takes into account original k-space measurements made by the MRI machine with neighborhood and spatial consistencies of the image in the spatial domain. This approach facilitates the difference in domain between MRI measurements made in the k-space, and the reconstruction results in spatial domain. An adaptive extension of the CD-SFCRF approach that takes into account regions of interest in the image and changes the CD-SFCRF neighborhood connectivity based on importance is presented and tested as well. Finally, a compensated CD-SFCRF approach that takes into account MRI machine imaging apparatus properties to correct for degradations and aberrations from the image acquisition process is presented and tested.

Clinical MRI data were collected from twenty patients with ground truth data examined and confirmed by an expert radiologist with multiple years of prostate cancer diagnosis experience. Compressive sensing simulations were performed and the reconstruction results show the CD-SFCRF and extension frameworks having noticeable improvements over state of the art methods. Tissue structure and image details are well preserved while sparse sampling artifacts were reduced and eliminated. Future work on this framework include extending the current work in multiple ways. Extensions including integration into computer aided diagnosis applications as well as improving on the compressive sensing strategy.

Acknowledgements

I would like to thank my mom, Jacqueline Wang, for her continued love and support through the easy times and the hard. I'd also like to thank my girlfriend, Allison Wang, for being my better half and for your love and understanding. Thank you both for always being there for me.

I would also like to thank my supervisor, Alex Wong. Thank you for giving me guidance and direction whenever I needed it. For chatting about all the random yet interesting things that expanded my horizon.

Finally, I would like to thank the Vision and Imaging Processing Group members. Thank you all for teaching me hard concepts like CRFs and MRFs, for patiently explaining things to me when I didn't understand. Thank you for all the conversations I had with you and the fun times we shared. I look forward to collaborating with you again in the future.

Dedication

This is dedicated to the ones I love.

Statement of Contribution

There are two journal papers (one submitted, one published) and one conference publication that make up the majority of this thesis. Edward Li (E.L.) was the major contributor and first author in all of these publications. The parts of the thesis that have been co-authored as well as co-author contributions are detailed in the following paragraphs.

The first paper has been submitted to BioMed Central in April 2016 and is titled *Sparse Reconstruction of Compressive Sensing MRI using Cross-Domain Stochastically Fully Connected Conditional Random Fields*. Sections 2.1, 2.2, and 2.3 in Chapter 2, Section 3.1 in Chapter 3 and Section 4.2.1 in Chapter 4 contains copied verbatim from this journal paper. Modifications have been made to these chapters to improve the flow of this thesis and to incorporate additional work done. For this journal paper, E.L., Mohammad Javad Shafiee (M.J.S.), Alexander Wong (A.W.), Farzad Khalvati (F.K.), and Masoom A Haider (M.A.H.) conceived and designed the concept. E.L., M.J.S. and A.W. designed and implemented the algorithm. F.K. and M.A.H. performed the data collection and medical data verification. E.L. and A.W. performed the experimental procedures. Finally, everyone contributed to the writing and editing of the paper.

The second paper is a published conference paper titled *Sparse Reconstruction of Compressive Sensing MRI using Cross-Domain Stochastically Fully Connected Conditional Random Fields* published by the ISMRM 2015 conference proceedings. Ideas and methodology formulations are taken from this paper and used in the thesis, more specifically Section 3.1 in Chapters 3 and Section 4.2.1 in Chapter 4. The contributions for this paper is similar to the previously mentioned journal paper with the same name, as the journal paper is written as an extension for this conference publication.

The third paper is a published journal paper titled *Compensated Diffusion Magnetic Resonance Imaging* published by Vision Letters journal in 2016. Sections 3.1.2 in chapter 3 and Section 4.2.3 in Chapter 4 contain copied verbatim from this conference paper. Modifications have been made to improve the flow of this thesis. E.L., M.J.S., Ameneh Boroomand (A.B.), F.K., A.W. and M.A.H. conceived and designed the concept. E.L., A.B. and A.W. implemented and tested the algorithm. F.K., and M.A.H. collected data and medical verification of results. Finally, everyone contributed to the writing and editing of the paper.

Table of Contents

List of Tables

List of Figures

Nomenclature

Y	ground truth set of states
$\hat{Y}$	estimated set of states from algorithm
X	set of observations made in k-space
C	set of clique structures
$\psi_u(.)$	unary potential function
$\psi_p(.)$	pairwise potential function
$N(i)$	set of neighboring nodes for node I
$C_p(i)$	clique for node i
$1^S_{\{i,j\}}$	stochastic indicator function
$P^s_{i,j}$	spatial information indicator
$Q^d_{i,j}$	inter-state data relation indicator
γ	stochastic sparsity factor
γ_t	pairwise sparsity factor for tumor
γ_p	pairwise sparsity factor for prostate
γ_o	pairwise sparsity factor for non-relevance
λ^u_j	unary feature function weight
λ^p_k	pairwise feature function weight
F	feature function in frequency domain
f	feature function in spatial domain
$\mathscr{F}(\cdot,\cdot)$	Fourier operator
$P(.)$	probability
σ	control variable for node pair weighting in clique
$G(.)$	graph function
V	set of nodes in graph
E	set of edges in graph
$L(i)$	label assigned to node i
l_i	each probably class label for i
a_k	attribute k that describe each instance of l_i
B	compensation function
D	degradation function
ζ	blur model characterization parameter

$\vec{x}$	measurement vector used in TV
$\vec{y}$	image vector used in TV
$\Phi(.)$	penalty function in TV
J	image lattice in spatial domain in l_0 minimization
$s \in S$	sites in image lattice in l_0 minimization
R	observation lattice in frequency domain in l_0 minimization
$k \in K$	sites in observation lattice in l_0 minimization
Ω	measurement operator in l_0 minimization
Ψ	sparsity domain in l_0 minimization
υ	relaxation term in l_0 minimization
ρ	homotopic approximation function in l_0 minimization
ϵ	error bound in l_0 minimization

Chapter 1

Introduction

1.1 Prostate Cancer

Cancer is a major health care concern for our society. In Canada and US for 2015 [1–3], 1,658,370 and 196,900 new cases of cancer were diagnosed with an expected mortality rate of nearly 35% and 40% respectively. Two out of every five Canadians should expect to develop cancer in their lifetime. Of all cancer cases 51% belong to the four major occurring types of cancer: Prostate cancer in men, breast cancer in women, lung and colorectal cancer in both sexes as show in Table 1.1.

Table 1.1: Cancer Statistics for US and Canada [1, 2]

	Occurrences		Mortality	
Cancer Type	US	Canada	US	Canada
Prostate	220,800	24,000	27,540	4,100
Breast Cancer	234,190	25,200	40,730	5,100
Lung	221,200	26,600	158,040	20,900
Colorectal	132,700	25,100	49,700	9,300

Prostate cancer specifically is the most commonly occurring cancer in Canadian and American men. One in eight men will be diagnosed in their lifetime [4]. However, early detection can greatly increase the successful treatment of prostate cancer and cancer in general. Prostate cancer in particular, it is a slow growing cancer and patients can live many

years without the cancer detected. In later stages of the disease, it becomes increasingly more difficult for successful treatment. Early detection can drastically increase the survival rate. Fast, efficient and accurate screening methods are highly desired to increase early detection rate and improve survival rate.

Current screening methods involve prostate-specific antigen (PSA) tests , digital rectal exams (DRE), prostate biopsy and transrectal ultrasounds [5]. However, reliability of these methods are hindered due to their limitations. PSA blood test results are usually influenced by a variety of factors including certain medicines, age, size of prostate and physical activities [5] and results can be inconsistent and thus unreliable. DREs, biopsies, and transrectal ultrasounds are invasive and cause great patient discomfort discouraging patients to partake in these examinations for early detection. Non-invasive and highly reliable screening methods are highly desired for early prostate cancer detection.

1.2 Magnetic Resonance Imaging

One non-ionizing, non invasive method for the early detection of prostate cancer is magnetic resonance imaging (MRI). MRI utilizes the body's natural magnetic properties to produce detailed images from any part of the body. Large magnets usually between 0.5 to 1.5 tesla, create strong magnetic fields to align the body's proton axes and cause the hydrogen nuclei to resonate. When the magnetic field is turned off, the body protons return to their original states. Different types of tissue behave differently and capturing the different responses yields images that doctors can use to help identify different tissue types. [6]

Additionally MRI can provide a wide variety of information through multi-parametric MRI (MP-MRI) with modalities including T1w, T2w, diffusion weighted imaging (DWI), dynamic contrast-enhanced MRI (DCE), correlated diffusion imaging (CDI) [7], and Apparent diffusion coefficient (ADC) maps. These modalities can all be used to help with more accurate and reliable diagnosis from MRI imagery.

Being non-ionizing and non-invasive in nature coupled with the abundant amount of diagnostic information available, MRI makes a reliable early screening method for prostate cancer.

1.3 Challenges for MRI

MRI does have it's challenges, most notably its' lengthy acquisition process ranging from 10 minutes to over 2 hours especially for MP-MRI. [8,9] Due to the long acquisition times,

the throughput of the system is low, hindering the practicality of MRI imagery for cancer diagnosis.

Compressive sensing has demonstrated to be an effective strategy for reducing MRI acquisition times by acquiring significantly fewer samples in k-space. A complete signal can be then reconstructed fully through sparse yet sufficient number of samples. [10–12]

Due to the reduction in the number of acquisitions at the imaging step, strong reconstruction algorithms are usually needed to facilitate for compressive sensing MRI. Sparse reconstruction algorithms need to provide accurate and high quality reconstruction results. Furthermore, reconstruction algorithms should be able to fully take advantage of available information in the reconstruction process.

Therefore, strong algorithms capable of fully utilizing available information to produce accurate and reliable reconstructions for compressive sensing MRI are highly desired. This can greatly increase the health care system throughput and the number of early detections for prostate cancer.

1.4 Thesis Contributions

The aim of this thesis is to introduce a new cross-domain stochastically fully connected conditional random field (CD-SFCRF) reconstruction approach to facilitate for compressive sensing MP-MRI. The CD-SFCRF reconstruction framework better utilizes available information by taking into account both original k-space measurement as well as spatially driven potentials to produce high quality reconstruction. The CD-SFCRF utilizes spatial and frequency information in a stochastically fully connected condtional random field graphical model to infer original information based on sparse MRI measurements. Results show quality reconstruction at low sampling rates while enhancing details in the region of interest. Furthermore, extensions on the framework are proposed which includes an adaptive CD-SFCRF (ACD-SFCRF) approach that learns intrinsic properties of tumorous, prostate as well as non-interest regions. Then the system adjust neighborhood stochastivity to increase the speed of the overall framework while retaining original quality and details in the region of interest. This thesis extends on the CD-SFCRF framework additionally by introducing a compensated CD-SFCRF (CCD-SFCRF) approach, this extension learns the intrinsic properties of MRI imagery and tries to compensate for the aberrations and distortions of the MRI machine. Results show enhanced compensated views for regions of interest with detail enhancement which allow for better tissue differentiation. The CD-SFCRF and its accompanying extensions are able to produce accurate and

clinically reliable reconstruction for compressively sensing MP-MRI while greatly reducing acquisition time increasing the throughput of the health care system.

1.5 Thesis Outline

Background information about the problem domain is introduced in Chapter 2, where state of the art compressive sensing strategies and sparse reconstruction algorithms are also compared. Mathematical background information is presented as well. In Chapter 3, the methodology behind the CD-SFCRF and its extensions are explained in detail. Chapter 4 focuses on presenting the experimental setup and demonstrating preliminary results from real patient data. Finally in Chapter 5, future work is discussed and conclusions are drawn from current work.

Chapter 2

Background Information

2.1 Compressive Sensing

Due to the vast amount of information acquired by current devices, a lot of the information is discarded specifically for cases such as lossy compression for images, sounds and technical data. Since there is no significant need for a complete set of data, compressive sensing strategies captures a sparse yet sufficient set of measurements representative of the original data [10–12]. Compressive sensing is mostly used for speeding the acquisition process. With a decreased set of acquired information, less time is required in the acquisition process to produce a meaningful image. Compressive sensing strategies are usually accompanied by strong reconstruction algorithms to infer missing information and reconstruct the original signal. The better the quality of the sparse reconstruction algorithm, the lower the compressive sensing rate and faster the acquisition process.

Compressive sensing has demonstrated to be an effective strategy for reducing MRI acquisition times by acquiring significantly fewer samples in k-space. A complete signal can be then be reconstructed fully through sparse, yet sufficient number of samples [10–12]. In MRI, compressive sampling strategies have been demonstrated to be highly effective at reducing acquisition time while maintaining image quality as different types of tissue structure have been shown to be sparse in certain domains [13]. Furthermore, different techniques have been proposed to improve the imaging process [14] as well as the reconstruction process [15–27] in compressive sensing. Due to the limited amount of data available through compressive sensing, advanced reconstruction algorithms are required to produce high quality reliable images. The ongoing challenges mainly span in improving

the reconstruction algorithms, improving the efficiency and quality of compressive sensing MRI.

Total Variation Reconstruction

A number of different methods have been proposed for sparse reconstruction of compressive sensing MRI [15–27]. As a notable example, Block *et al.* [18] proposed an iterative image reconstruction technique using a modified total variation (TV) [24,25] constraint for sparse reconstruction of compressive sensing brain MRI. The total variational reconstruction method iteratively solves for image vector $\vec{y}$ that optimizes matrix A for this known forward problem :

$$\vec{x} = A\vec{y} \tag{2.1}$$

where $\vec{x}$ is the original observations data vector (Fourier transform of MRI acquisitions) and $\vec{y}$ is the image vector (estimation of image from data vector). Because of the ill posed nature and scale of the problem the TV approach optimizes for A using:

$$\vec{y} = \underset{\vec{y}}{\operatorname{argmin}}\, \Phi(\vec{y}) \tag{2.2}$$

$$\Phi(\vec{y}) = \frac{1}{2}||A\vec{y} - \vec{x}||_2 + \sum_j \lambda_j \psi_j(\vec{y}) \tag{2.3}$$

This becomes an iterative optimization problem to optimize an l_2 norm for A based on a penalty function $\psi_j(.)$ with weight λ_j for all j. The optimal A should minimize the penalty functions based on the result vector $\vec{y}$. The result vector that optimizes these conditions is finally returned. Note that the observations $\vec{x}$ and the reconstructed image $\vec{y}$ are both in the spatial domain.

l_0 Minimization

Another notable reconstruction algorithm is the l_0 minimization technique. Trzasko *et al.* [19] introduced a homotopic l_0 minimization method for the sparse reconstruction of compressive sensing spinal MRI. Wong *et al.* [16] extended upon this idea to a regional

sparsified domain for the sparse reconstruction of breast MRI. A similar technique was also demonstrated by Qu *et al.* using combined sparsifying transforms and smoothed l_0 norm minimization [17], where they showed that the use of combined transforms can improve image quality compared to the reconstructed images from compressive sensing MRI when compared to methods using a single sparsifying transform.

The l_0 minimization technique models k-space observations X as a set of sites $k \in K$ in discrete k-space lattice J and their transformed image Y as a set of sites $s \in S$ in a discrete spatial lattice R. Here $\hat{j}(s)$ and $\hat{R}(k)$ are estimates of the signals $j(s)$ and $R(k)$ in their respective domains with their relationship expressed by 2.4:

$$j(s) = \mathscr{F}^{-1}[\Omega R(k)] \tag{2.4}$$

where Ω is a measurement operator to indicate positions of true measurements and $\mathscr{F}(\cdot,\cdot)$ is the Fourier operator (used later as well).

Using the idea that MRI images are inherently sparse in sparse domain Ψ, the l_0 minimization models the inverse problem of getting our image $\hat{Y}$ as shown in Eq 2.6 :

$$\hat{Y} = \hat{j}(s) \tag{2.5}$$

$$\hat{j}(s) = \underset{j(S)}{\operatorname{argmin}} ||\Psi j(s)||_0 \qquad s.t. \qquad \Omega\hat{R}(k) = \Omega R(k) \tag{2.6}$$

where $\Omega\hat{R}(k) = \Omega R(k)$ enforces data fidelity.

The homotopic l_0 minimization tries to solve the above problem iteratively as the constrained l_0 problem is nondeterministically polynomial-time hard (NP-hard) [16]. The iterative method introduces a relaxation factor υ to model the difference between the approximated homotopic l_0 norm and the actual l_0 norm in the approximation function $\rho(.)$. Finally, the data fidelity condition is now approximated as a l_2 norm with error bound ϵ. This is shown in 2.8 :

$$\hat{j}(s) = \lim_{\upsilon \to 0} \underset{j(s)}{\operatorname{argmin}} \sum_S \rho(|\Psi j(s)|, \upsilon) \tag{2.7}$$

$$s.t. \qquad ||\Omega\hat{R}(k) - \Omega R(k)||_2 < \epsilon \tag{2.8}$$

Note that the relaxation factor υ can greatly affect the convergence rate of this iterative approach.

2.2 Conditional Random Fields and Graph Theory

An area that is little explored but can be significantly beneficial is the applications of random field modeling for improved sparse reconstruction of compressive sensing MRI. Random field modeling such as Markov random fields (MRFs) [28, 29] and conditional random fields (CRFs) [30] have long been shown to be powerful tools for incorporating spatial context within a probabilistic graphical modeling framework.

Markov random fields (MRF) [28, 29] are undirected graphs that model relationships between nodes in the graph. Nodes in Markov random fields must satisfy the Markov property that the conditional probability distribution of future states in the process depends only upon the present state and not on the sequence of events that precede it. This property can be specifically useful in imaging applications to model pixels and their represented states. For MRI imaging applications we are given observations (MRI machine sparse acquisitions) and we attempt to infer the label associated with the observation (reconstructed image representative of patient condition). Markov random fields are generative models that learn the model of the joint probability $P(X, Y)$ of inputs X and their labels Y and then use Bayesian rules to calculate $P(Y|X)$ and then pick the label Y with the highest probability [31].

Conditional random fields (CRFs) [30] are similar to MRFs. The difference is that a CRF is discriminative graphical model, which models the posterior probability $P(Y|X)$ directly [31]. This is an advantage as modeling the posterior solves the inference problem directly. It is better to solve the problem directly than solving a more general problem as an intermediate step (such as modeling the joint probability) [32]. CRFs have demonstrated a success in machine learning for classification and labeling problems. Because a CRF takes into account relationships between observations and neighborhood consistencies, it can be especially useful for imaging applications.

Shafiee *et al.* proposed a stochastically fully connected conditional random field model (SFCRF) that greatly improves the number of connections in the CRF graphical model for better modeling of the posterior while at the same time maintaining computational efficiency [33]. This model has shown the potential to take a larger neighborhood context into consideration for better enhancement of structural details in the image. Furthermore, the SFCRF maintains computational efficiency as well by stochastially determining the connection between nodes in the graph. This ensures that nodes with low probability of connectivity are not considered. This model has great potential for sparse reconstruction of compressive sensing MRI.

2.3 Shortcomings of Existing Methods

The existing state of the art reconstruction algorithms are mostly focused on the spatial domain. Additionally, current sparse reconstruction techniques are limited to the modeling that they incorporate. For example, in total variational approaches [18], image reconstruction can yield block-like features in the image due to total variation constraint. In homotopic l_0 approaches, run time is hindered by the convergence rate to the l_0 norm and thus the reconstruction has to be tuned to reduce runtime. Original MRI measurement are made in the k-space, so it is beneficial to directly utilize this information for better quality reconstruction. The biggest hurdle for compressive sensing MRI is that all MRI measurements are made in k-space, whereas the reconstructed image exists in the spatial domain. Most random field models tend to model information in a singular domain, these models are insufficient for the sparse reconstruction of compressive sensing MRI. This is further complicated by MRI measurement in the k-space being sparse and incomplete making it difficult to leverage current random field models. Therefore a probabilistic graphical model that can consolidate the fact that partial measurements are made in a different domain than the desired states of the reconstructed image is needed to truly leverage the power of random field modeling for spare reconstruction for compressive sensing MRI.

2.4 Summary

Compressive sensing has demonstrated the ability to reconstruct complete signals using sparse yet sufficient measurements. Compressive sensing strategies are often accompanied by strong reconstruction algorithms. Additionally, random field modeling has potential for applications in improving sparse reconstruction of compressive sensing MRI. The main challenge of compressive sensing MRI is that sparse observations are made in a different domain (k-space) than the reconstructed image (spatial domain). Many state of the art reconstruction algorithms are in a singular domain. In addition, current random field models tends to model in a singular domain. Therefore to utilize random field modeling for the sparse reconstruction of compressive sensing MRI, a model that accounts for observations and states being in different domains is required. This paper proposes such a Cross-domain stochastically fully connected conditional random field approach that takes into account the multi-domain nature of compressive sensing MRI to improve sparse reconstruction results. With a strong reconstruction algorithm, compressive sampling rates can be further reduced to decrease MP-MRI acquisition times and increase the number of early detection for cancer.

Chapter 3

Methodology

The cross domain stochastic fully connected conditional random field (CD-SFCRF) is first introduced and lays down the foundation for how to utilize original k-space measurements within a CD-SFCRF approach. Two extensions are proposed, the adaptive CD-SFCRF (ACD-SFCRF) tries to speed up the reconstruction by first learning about the feature space and then classifying regions of interest to increase neighborhood connectivity and lower neighborhood connectivity in regions of non interest. Second, a compensated CD-SFCRF (CCD-SFCRF) approach is proposed to compensate the image based on intrinsic properties of the imaging system. This compensation corrects for degradations caused by the imaging apparatus and enhances image details.

3.1 CD-SFCRF

In MRI, measurements are made in the k-space [34], with the lower frequency coefficients in the k-space containing coarse-grained contrast information while higher frequency coefficients contain fine-grained image detail information. The MRI measurements from the k-space are transformed into the spatial domain to form the reconstructed MRI image. Most compressive sensing strategies [12, 19] sparsely sample the k-space to reduce image acquisition time significantly. Therefore, to fully utilize available information in the reconstruction process, data-driven constraints in the k-space domain and data and spatial driven constraints in the spatial domain would be highly beneficial in improving image reconstruction quality from compressive sensing MRI.

Motivated by this, the proposed cross-domain stochastically fully connected conditional

random field (CD-SFCRF), introduced here for the purpose of sparse reconstruction of compressive sensing MRI, extends upon the seminal work on stochastically fully connected conditional random fields (SFCRF) [33] to facilitate for this cross-domain optimization. Let us first discuss the concept of SFCRFs briefly for context to build CD-SFCRFs. SFCRFs are fully-connected conditional random fields with stochastically defined cliques. Unlike traditional conditional random fields (CRFs), where nodal interactions are deterministic and restricted to local neighborhoods, each node in the graph representing a SFCRF is connected to every other node in the graph, with the cliques for each node stochastically determined based on a distribution probability. Therefore, the number of pairwise cliques might not be the same as the number of neighborhood pairs as in the traditional CRF models. By leveraging long-range nodal interactions in a stochastic manner, SFCRFs facilitate improved detail preservation while maintaining similar computational complexity as CRFs, which makes SFCRFs particularly enticing for the purpose of improved sparse reconstruction of compressive sensing MRI. However, here the problem is to reconstruct an MRI image in the spatial domain while the available measurements are made in k-space domain. Like most CRF models, SFCRFs cannot be leveraged directly for this purpose. Motivated by the significant potential benefits of using SFCRFs in improving reconstruction quality of compressive sensing MRI, we extend the SFCRF model into a cross-domain stochastically fully connected conditional random field (CD-SFCRF) model that incorporates cross-domain information and constraints from k-space and spatial domains to reconstruct the desirable MRI image from sparse observations in k-space.

The main goal here is to reconstruct the spatial domain image Y given original sparsely sampled k-space observations X. We model the conditional probability $P(Y|X)$ of the full state set Y (estimated by $\hat{Y}$) in spatial domain given the set of sparse measurements X in k-space, which can be written as:

$$P(Y|X) = \frac{1}{Z(X)} \exp(-\psi(Y|X)) \tag{3.1}$$

where $Z(X)$ is the normalization function to constrain probabilities between $[0, 1]$ and $\psi(.)$ is a combination of unary and pairwise potential functions:

$$\psi(Y|X) = \sum_{i=1}^{n} \psi_u(y_i, X) + \sum_{\varphi \in C} \psi_p(y_\varphi, X) \tag{3.2}$$

Here $y_i \in Y$ is a single state in the set $Y = \{y_i\}_{i=1}^n$, $y_\varphi \in Y$ encodes a clique structure in the set C, and $X = \{x_j\}_{j=1}^n$ represents the observations (radially sub-sampled frequency coefficients) in the frequency domain (k-space). n is the total number of nodes in the

graph. The unary potential ψ_u is enforced in the k-space while the pairwise potential ψ_p is applied in the spatial domain. The unary potential enforces original observations to preserve data fidelity. Since the available observations are captured in k-space in MRI, the model must be formulated in a way to be consistent in both k-space and spatial domain.

The pairwise potential, has to be in the spatial domain to better preserve image detail since neighboring coefficients in the k-space does not contain any meaningful spatial or data consistencies to be utilized by the pairwise potential. Therefore, the optimal way to fully utilize available data within this random field model is to formulate the unary potential in the k-space and the pairwise potential in the spatial domain. This is because working with a MRI machine, the output signal is in the k-space. There is no spatial information in the k-space.

One of main differences between the proposed CD-SFCRF framework from conventional CRF models is to incorporate long-range information in the model and preserve boundaries and image structural properties more effectively which is important here due to sparse available observation. To capture long-range information, CD-SFCRF assumes fully connected neighboring structure for the underlying graph in which each node i has a set of neighbors $N(i)$, where

$$N(i) = \Big\{ j | j = 1 : n, j \neq 1 \Big\} \tag{3.3}$$

where $|N(i)| = n - 1$ and includes all other nodes in the graph as neighbors of node i. Here the pairwise clique structures are utilized such that:

$$C = \Big\{ C_p(i) \Big\}_{i=1}^{n} \tag{3.4}$$

$$C_p(i) = \Big\{ (i,j) | j \in N(i), 1^S_{\{i,j\}} = 1 \Big\}. \tag{3.5}$$

The active cliques in the inference procedure are determined by the stochastic indicator function $1^S_{\{i,j\}} = 1$. The indicator function decides whether or not nodes can construct a clique, $C_p(i)$, for node i. This stochastic indicator function combines spatial and data driven information to model the probability distribution of informative cliques which informative cliques have higher probability to participate in the inference. This combination of spatially driven and data driven probabilities can be expressed as:

$$1^S_{\{i,j\}} = \begin{cases} 1 & Q^d_{i,j} \geq \gamma \\ 0 & \text{otherwise} \end{cases} \tag{3.6}$$

$1^S_{\{i,j\}} = 1$ incorporates the data relationship in the image between the states $Q^d_{i,j}$ while γ is the real value sparsity factor between (0 and 100) used to determine the number of active cliques in the inference. The set of active cliques are obtained to extract pairwise potentials in Eq. 3.2. $Q^d_{i,j}$ is defined as :

$$Q^d_{i,j} = exp((\sigma) - (\mathscr{F}[x_i] - \mathscr{F}[x_j])^2) \cdot 100 \tag{3.7}$$

$$\tag{3.8}$$

where σ is a control variable for the amount of weighting node pairs in the clique $\varphi = \{i, j\}$.

As mentioned before $\psi(\cdot)$ in Eq. 3.2 is the combination of two potential functions $\psi_u(.)$, the unary potential and $\psi_p(.)$, the pairwise potential. These potential functions are formulated with their corresponding weights λ, respectively as:

$$\psi_u(Y, X) = \sum_{j=1}^{K} \lambda^u_j F_j(Y, X) \tag{3.9}$$

$$\psi_p(y_\varphi, X) = \sum_{\{y_i, y_j\} \in y_\varphi, k=1}^{K'} \lambda^p_k f_k(y_i, y_j, X) \tag{3.10}$$

where λ controls the importance of each feature function in the energy formulation and it is calculated in the training stages. Although it is possible to provide several arbitrary feature functions to model the conditional probability $P(Y|X)$, here two feature functions are provided to formulate the image reconstruction for the purpose of sparse reconstruction from compressive sensing MRI. The conditional distribution of Y given X is trained to promote/suppress different features in both the unary and pairwise potentials. Higher λ^u_j values promotes a higher reinforcement of original observations while high λ^p_k values promotes higher consideration of spatial and data driven neighborhood constraints. In Eq. 3.9, F refers to the frequency domain potential function. The unary potential is calculated in the k-space while the pairwise remains in the spatial domain. This is the novelty of the CD-SFCRF and facilitates for better preservation of fine tissue details and contrast in the reconstructed image. The unary potential is in the k-space and the simplest unary function is the l_1-norm. The unary potential function $F_j(y_i, X)$ can be formulated as:

$$F_j(Y, X) = \sum_{\omega=-\frac{\pi}{2}}^{\frac{\pi}{2}} \mathscr{F}^{-1}(Y, \omega) - x_\omega \tag{3.11}$$

where $\mathscr{F}(\cdot, \cdot)$ is the Fourier operator and returns the k-space coefficient corresponding to frequency ω. Based on this formulation, the unary potential is enforced in the k-space and in the inferencing step the model tries to estimate image Y to be consistent to the original k-space observation $X = \{x_\omega\}_{\omega=-\frac{\pi}{2}}^{\frac{\pi}{2}}$.

The pairwise function tries to penalize the intensity differences between nodes in the spatial domain, similar nodes will have more influence on each other while different nodes will have their differences highlighted. The pairwise function $f_k(y_i, y_j, X)$ can be formulated as:

$$f_k(y_i, y_j, X) = \exp\left(\frac{-(y_i - y_j)^2 \cdot (\mathscr{F}[x_i] - \mathscr{F}[x_j])^2}{3\sigma^2}\right) \tag{3.12}$$

where σ is the same σ in 3.8. Contrary to the unary potential, the pairwise potential is enforced in the spatial domain.

Graph Representation for CD-SFCRF

Graph $G(V, E)$ (Figure 3.1) is the realization of the CD-SFCRF where V is the set of nodes of the graph representing states $Y = \{y_i\}_{i=1}^n$, E is the set of edges in the graph. Observations $x_i \in X$ are made in the k-space domain. Our final state estimations $\hat{Y}$ (approximation of Y) are in the spatial domain (image). Figure 3.1 shows the graphical representation how the spatial and k-space domain are incorporated to model the conditional probability $P(Y|X)$. x_i comes from the set sparse measurements X in the k-space. In the inference procedure the k-space observations are transformed into the spatial domain using the Fourier transform to compute the pairwise potentials. Pairwise potentials are calculated in the spatial domain (Eq. 3.12) and transformed back into the k-space using the inverse Fourier transform to combine with the unary potential and perform data fidelity (Eq. 3.11). For different types of MRI data, different sparse sampling patterns can be used. Furthermore, pairwise connectivity can be trained for specific types of details and tissue structure.

The proposed CD-SFCRF framework utilizes consistencies from the spatial domain through the pairwise potential in conjunction with k-space information through the unary

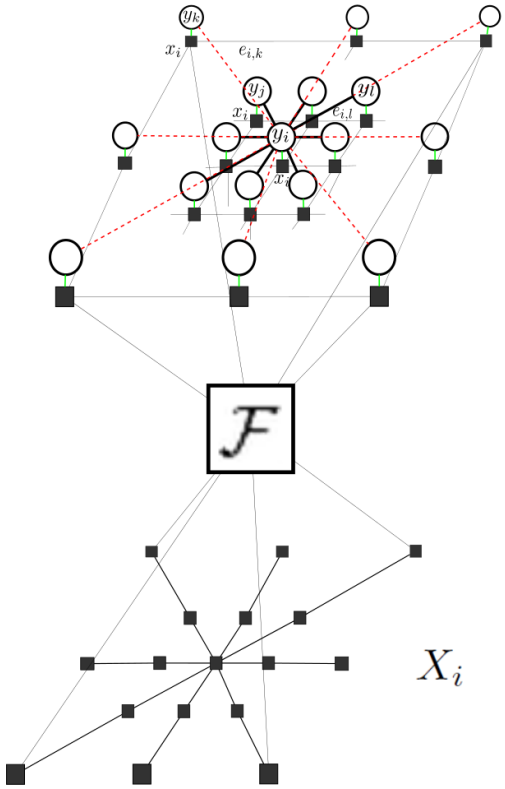

Figure 3.1: Realization of CD-SFCRF graph. X_i represents original observations made in the k-space, x_i represents spatial domain representation of the k-space measurements and y_i represent states. $\mathscr{F}(\cdot,\cdot)$ denotes the Fourier operator used in transforming k-space observations into the spatial domain. Connectivity is determined based on probability distributions. Nodes with higher connectivity have solid black edges while lower probable connections are represented as dashed red lines

potential. A combination of the two potentials is enforced simultaneously. The unary potential utilizes original observations in the k-space, while the pairwise potential utilizes the spatial domain representation of the observation/state information and calculates pairwise potentials for nodes in the spatial domain. This allows CD-SFCRF to take advantage of the lower computation complexity introduced by the stochastically fully-connected random field model, while leveraging the original k-space observations in improving signal fidelity.

3.1.1 ACD-SFCRF

The adaptive CD-SFCRF (ACD-SFCRF) approach takes into account the importance of regions in the spatial domain. Having classification information about the different regions of interest, the neighborhood connectivity of the CD-SFCRF can be tuned. This is performed in the spatial domain as the neighborhood connectivity only applies in the CRF pairwise potential calculated in the spatial domain. Mathematically this can be formulated as follows.

Eq 3.13, shows the different levels of stochastic connectivity of the ACD-SFCRF. $L(i)$ is the label assigned to node i.

$$\gamma(.) = \begin{cases} \gamma_t & L(i) = \text{tumor} \\ \gamma_p & L(i) = \text{prostate} \\ \gamma_o & \text{otherwise} \end{cases} \tag{3.13}$$

$$\text{where } \gamma_t > \gamma_p > \gamma_o$$

Pairwise connectivity thresholds γ_t, γ_p, and γ_o (real values between 0 and 100) were tested and set accordingly for tumor, prostate and others class. Tumors are areas of highest importance. Therefore, these areas have the highest connectivity for the highest level of neighborhood enforcement. Prostate areas are second in importance and connectivity. Other pixels are irrelevant and thus the connectivity can be lowered for these pixels. This increases the algorithm processing speed. $L(i)$ is a Bayesian classifier function following the naive Bayes constraint is defined by :

$$L(i) = \arg\max_{l_i \in L} P(l_i | a_1, a_2, ...a_k) \tag{3.14}$$

$$= \arg\max_{l_i \in L} P(l_i) P(a_1, a_2, ...a_k | l_i) \tag{3.15}$$

$$\tag{3.16}$$

following Bayes theorem (Eq. 3.18), Eq. 3.14 is expressed as Eq. 3.15. Finally, the naive independence assumption in Eq. 3.19 is used and the classifier assumes the final form (Eq. 3.19). Notice $P(a_1, a_2, ...a_k)$ is constant given the input and can thus be omitted in Eq. 3.15. Bayes theorem and the naive independence assumption is defined by :

$$P(l_i|a_1, a_2, ...a_k) = \frac{P(l_i)P(a_1, a_2, ...a_k|l_i)}{P(a_1, a_2, ...a_k)} \tag{3.17}$$

$$\tag{3.18}$$

$$P(a_1, a_2, ...a_k|l_i) = \prod_k P(a_k|l_i) \tag{3.19}$$

The terms $< a_1, a_2, a_3, ...a_k >$ represent the set of attributes that describe each instance of l_i. The label l_i indicate each probable class label for node i. The naive Bayesian classifier finds the class label that maximizes the optimal Bayes probability in Eq 3.15. However, following the naive Bayes assumption as the learning data set is limited and does not contain every possible attribute that describes l_i, the naive Bayes assumption is taken in Eq 3.19, the classifier $L(i)$ assumes the final form of Eq 3.21.

$$L(i) = \arg\max_{l_i \in L} P(l_i) \prod_k P(a_k|l_i) \tag{3.20}$$

$$\tag{3.21}$$

Different estimates of $P(l_i)$ gives different variations of the naive Bayes classifier. For the maximum a-priori classification $P(l_i)$ is calculated based on the training data to provide general distribution of each label. For the maximum likelihood case, $P(l_i)$ is equal for all labels. The ACD-SFCRF utilizes a higher $P(l_i)$ for regions of interest compared to regions of non-interest.

Graph Representation for ACD-SFCRF

The graph representation of the ACD-SFCRF changes slightly from the CD-SFCRF to incorporate the change in neighborhood connectivity as shown in Figure 3.2. Each node now has a classification label. The different classification results varies the neighborhood connectivity of each node. This further promotes high connectivity between nodes with similar labels because nodes with low connectivity would favor connections to similar nodes and nodes with high connectivity have more neighborhood information to utilize.

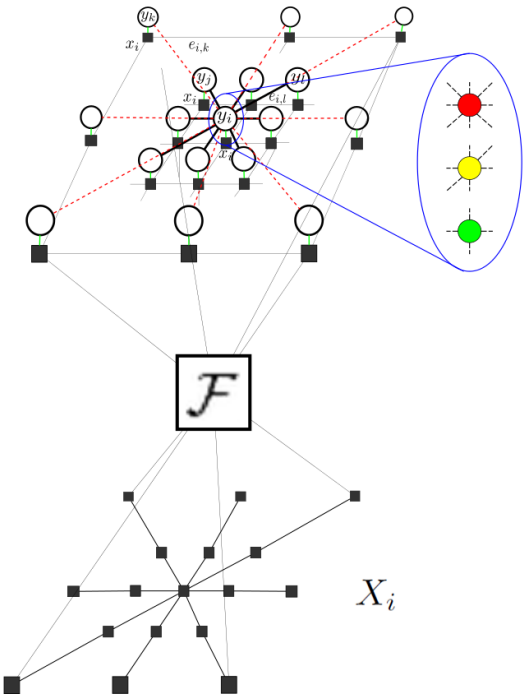

Figure 3.2: Realization of ACD-SFCRF graph. X_i represents original observations made in the k-space, x_i represents spatial domain representation of the k-space measurements and y_i is state in set Y. $\mathscr{F}(\cdot,\cdot)$ denotes the Fourier operator used in transforming k-space observations into the spatial domain. Connectivity is determined based on probability distributions and classification from learning. Nodes with higher connectivity have solid black edges while lower probable connections are represented as dashed red lines. Center nodes with higher importance(red) have higher neighborhood connectivity while nodes with lower importance(green) have lower neighborhood connectivity.

3.1.2 CCD-SFCRF

The compensated CD-SFCRF (CCD-SFCRF) includes an additional compensation stage that takes into account the intrinsic properties of the imaging system to compensate for

degradations caused by the imaging apparatus.

First, a calibration process is performed to quantitatively characterize the intrinsic properties of the MRI apparatus in the form of a compensation function B. This information is available through testing on phantom data. The measured sparse signal X, along with B, as well as CD-SFCRF reconstruction are then used to form a CCD-SFCRF image $\hat{Y}$ that tries to estimate the full set of states Y.

The CCD-SFCRF slightly alters the unary potential calculation by introducing the compensation function B, as in Eq 3.22. The pairwise potential changes slightly as well in Eq 3.23

$$\psi_u(y_i, X) = x_i - \mathscr{F}^{-1}[B(y_i)] \tag{3.22}$$

$$\psi_p(y_i, y_j, X) = e^{(-\frac{(\mathscr{F}[x_i]-\mathscr{F}[x_j])^2}{\sigma})}(y_i - y_j) \tag{3.23}$$

The unary potential is calculated after the estimate of y_i has been calculated through the CD-SFCRF reconstruction. The compensated y_i is then used to calculate the unary potential by enforcing original measurements x_i for node i.

The compensation function B is formulated in Eq 3.24:

$$B(y_i) = \frac{e^{-\zeta}\zeta_i^y}{y_i!} \tag{3.24}$$

the parameter ζ is a learned parameter that best suits the blur model. This parameter is learned through testing with phantom MRI data.

With the additional compensation involved, enhancement of tissue structures and image details can be achieved.

3.2 Implementation

An implementation of the proposed CD-SFCRF framework for the purpose of sparse reconstruction from compressive sensing MRI is illustrated in Figure 3.3. Here, an iterative gradient descent optimization approach is employed, and can be described as follows. First, the original compressive sensing MRI data in k-space is transformed to the spatial domain

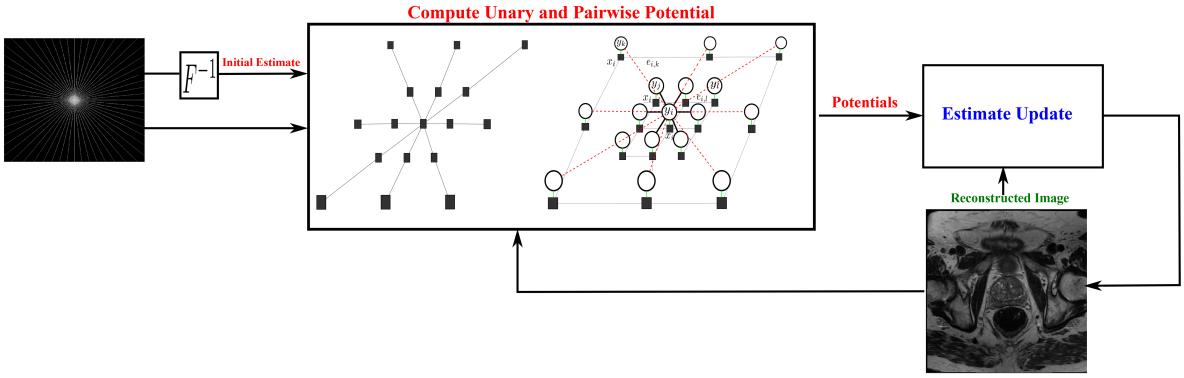

Figure 3.3: Optimization framework of the proposed CD-SFCRF framework for sparse reconstruction from compressive sensing MRI. The left image represents spiral sampled k-space measurements. The right image in the loop represents the final result the algorithm tries to achieve.

to provide an initial estimate of the reconstructed image. Second, the gradient of the unary and pairwise energy potentials in Eq. 3.9 and Eq. 3.10 is computed, where the unary data driven consistencies with respect to the original observations are enforced in the k-space, and spatial and data driven consistencies are enforced in the spatial domain. Third, the estimate of the reconstructed image is updated based on the previous estimate and the computed gradient. The second and third steps of this process is repeated until convergence.

With the addition of the ACD-SFCRF, two implementation details are added. The first being a classification of the reconstructed image in step one after transforming k-space measurements into the spatial domain. This initial classification changes the level of pairwise connectivity when calulating pairwise energy potentials in step two. The classification is done a singular time while the different levels of pairwise connectivity is applied at every iteration.

The addition of the CCD-SFCRF introduces an additional compensation step after enforcing pairwise potentials in step two. After compensation the unary potential is then calculated. This is based on original k-space measurements and compensated image (transformed into k-space). The compensation step is performed at every iteration as well.

Chapter 4

Experimental Setup and Results

The following sections outlines the experimental setup for evaluating the efficacy of the CD-SFCRF and its extension frameworks.

4.1 Expermental Setup

4.1.1 Patient Data and Ethics

To test the efficacy of the proposed CD-SFCRF framework and extension frameworks within a clinical scenario, MRI data of 20 patients (17 with cancer and 3 without cancer) were acquired using a MRI machine at Sunnybrook Health Sciences Centre, Toronto, Ontario, Canada. All data was obtained retrospectively under the local institutional research ethics board (Research Ethics Board of Sunnybrook Health Sciences Centre). For each patient, the following MP-MRI modalities were obtained (Table 4.1): T2w and DWI. The patients' age ranged from 53 to 83. Table 4.1 summarizes the information about the 20 patients' datasets used in this study, which includes displayed field of view (DFOV), resolution, echo time (TE), and repetition time (TR). Furthermore, ground truth labels for tumor, prostate and other areas are provided as well. The ground truth labels are created by radiologist from Sunnybrook Health Sciences Center with multiple years of experience.

Table 4.1: Description of the prostate T2w and DWI images

Modality	DFOV (cm^2)	Resolution (mm^3)	TE (ms)	TR (ms)
T2w	22×22	$0.49 \times 0.49 \times 3$	110	4,687
DWI	20×20	$1.56 \times 1.56 \times 3$	61	6,178

4.1.2 MRI Machine Parameters

Patients were scanned using a Philips Achieva 3.0T machine. The axial single-shot echo-planner DWI sequences used from the cases were performed with the following imaging parameters: TR ranged from $3336 - 6178ms$ with a median of $4890ms$, and TE ranged from $61 - 67ms$ with a median of $61ms$. the resolution of the signal acquisitions ranged from $1.36 \times 1.36mm^2$ to $1.67 \times 1.67mm^2$, with a median of $1.56 \times 1.56mm^2$. Slice thickness ranged from $3.0 - 4.0mm$ with a median of $3.5mm$. The display field of view (DFOV) ranged from $20 \times 20cm^2$to$24 \times 24cm^2$ with a median $24 \times 24cm^2$. The number of b-values in each case is either 4 or 6 with the highest b-value being $b = 1400s/mm^2$.

4.1.3 Compressive Sensing Simulation

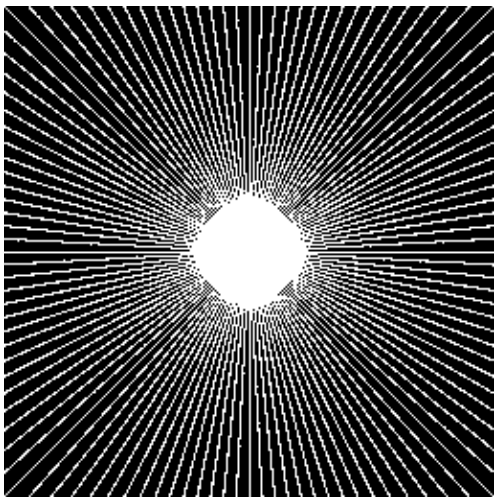

Figure 4.1: Radial k-space sampling pattern at 32% percentage sampled.

To test the reconstruction quality of the algorithm, fully sampled phantom and patient data was sub-sampled and reconstructed. The fully sampled data was used as ground

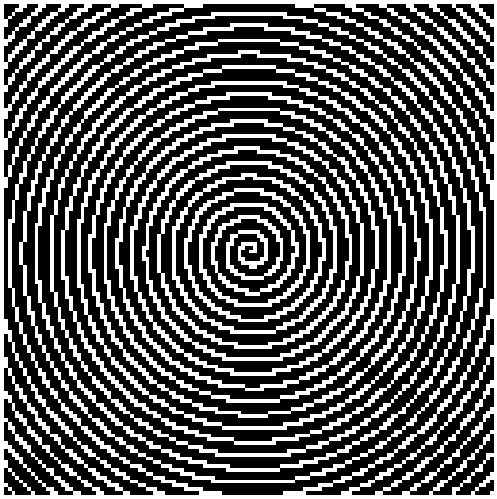

Figure 4.2: Radial k-space sampling pattern at 32% percentage sampled.

truth to compare with reconstructed data. Multiple k-space sampling patterns were used to simulate the compressive sensing of MRI [35, 36]. The two sampling patterns used were the radial and spiral sampling pattern shown in Figures 4.1 and 4.2 respectively. Multiple k-space sub-Nyquist [37] sampling ratios were explored as well ranging from 5 % to 40 %.

4.1.4 Evaluation Metrics

Quantitative analysis was performed using two metrics. The first being peak signal-to-noise ratio (PSNR) [38]. PSNR calculates the ratio between the maximum power of a signal and the power of the noise/degredation corrupting the fidelity of the signal. PSNR is usually expressed in a logarithmic decibel scale and can be calculated in Eq 4.1 as :

$$PSNR = 10 \cdot \log_{10} \left(\frac{MAX_I^2}{\sqrt{MSE}} \right) \tag{4.1}$$

$$MSE = \frac{1}{mn} \sum_{i=0}^{m-1} \sum_{j=0}^{n-1} [Y(i,j) - \hat{Y}(i,j)] \tag{4.2}$$

Where Y is the noise free image (ground truth) and $\hat{Y}$ is the approximation (reconstruction result).

Additionally, to test the ACD-SFCRF, algorithm runtime is captured in seconds(s) to evaluate the speed improvements that can be achieved, ten fold cross validation is performed to test classifier robustness and accuracy measured in percentages (%).

4.2 Detailed Results

4.2.1 CD-SFCRF results

To evaluate the efficacy of the proposed CD-SFCRF framework for sparse reconstruction of compressive sensing MRI, a comparative evaluation analysis was performed alongside a baseline l_2 minimization (L_2) reconstruction method, and a state-of-the-art homotopic l_0 minimization (HL_0) [19] reconstruction method. The tested methods are compared quantitatively though peak signal-to-noise (PSNR) analysis, and qualitatively via visual assessment. All tested methods are implemented based on the original literature, with optimal parameters used in this study. All tested methods are run until convergence.

Figure 4.3 shows the PSNR vs. sampling percentage plots for the tested methods for the phantom MRI data. The proposed CD-SFCRF framework achieved noticeable PSNR improvements over the other tested methods at all tested sampling percentages. The CD-SFCRF produced improvements of up to $4dB$ over HL_0 and $7dB$ over L_2 in low sampling conditions. It can be observed that as sampling percentage increases, the performance differences decreases. This is due to the fact that as the sampling percentage increases the amount of available measurements increases, and as such the level of reconstruction quality improvements that can be achieved will naturally decrease given the amount of available information becomes increasingly sufficient for high quality reconstruction. The ability of the CD-SFCRF framework to produce high quality reconstruction at very low sampling rates can be demonstrated visually as well.

Tables 4.2, 4.3, and 4.4, show the PSNR results for the three reconstructed methods for the T2w, DWI, as well as ADC map images for the patient experiments at different sampling rates. It can be observed that the proposed CD-SFCRF framework achieved the greatest PSNR improvements for the lowest sampling rate (i.e., 17%) where for T2w, CD-SFCRF improves PSNR by $1.78dB$ and $1.12dB$ over the L_2 and HL_0 methods, respectively. For DWI, CD-SFCRF improves PSNR by $1.85dB$ and $0.28dB$ over the L_2 and HL_0 methods, respectively. Interestingly for ADC maps, the best improvements in PSNR are achieved for the highest sampling rate (47%) where for CD-SFCRF improves PSNR by $4.44dB$ and $0.21dB$ over the L_2 and HL_0 methods, respectively.

Table 4.2: Calculated PSNR for T2w image for the patient experiments across different methods

Percentage Sampled (%)	L_2 (dB)	HL_0 (dB)	CD-SFCRF (dB)
17	25.56	26.22	**27.34**
32	28.39	28.80	**29.72**
47	30.42	30.80	**31.23**

Table 4.3: Calculated PSNR for DWI images for the patient experiments across different methods

Percentage Sampled (%)	L_2 (dB)	HL_0 (dB)	CD-SFCRF (dB)
17	26.90	28.46	**28.75**
32	31.92	33.39	**33.61**
47	36.45	37.85	**37.99**

Figure 4.4 shows the visual comparison between between the reconstructed images produced using the proposed CD-SFCRF framework compared with that produced using

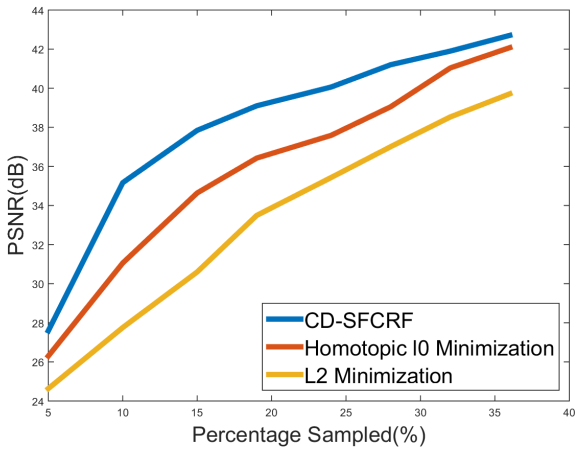

Figure 4.3: PSNR vs. sampling percentage plots for the tested methods for the phantom MRI data at different sampling percentages.

Table 4.4: Calculated PSNR for ADC images for the patient experiments across different methods

Sampling Rate (%)	L_2 (dB)	HL_0 (dB)	CD-SFCRF (dB)
17	17.20	19.35	**19.50**
32	18.05	21.66	**21.72**
47	18.72	22.94	**23.16**

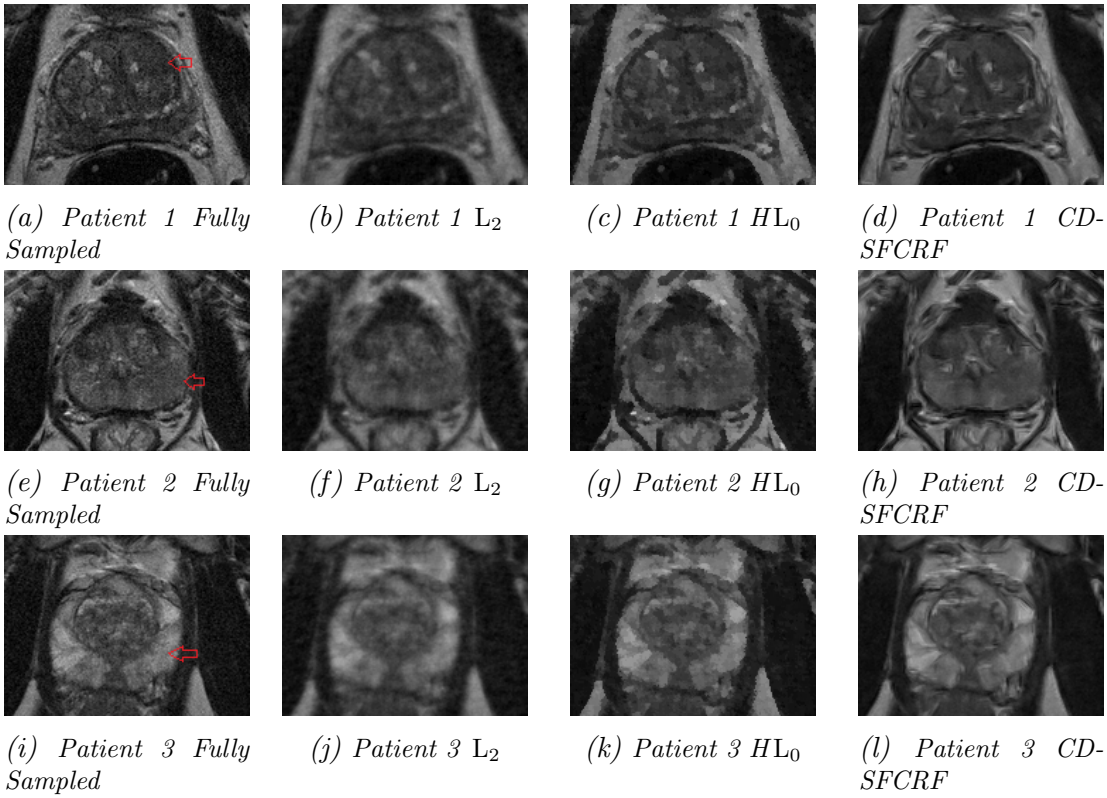

(a) Patient 1 Fully Sampled *(b) Patient 1* L_2 *(c) Patient 1 H*L_0 *(d) Patient 1 CD-SFCRF*

(e) Patient 2 Fully Sampled *(f) Patient 2* L_2 *(g) Patient 2 H*L_0 *(h) Patient 2 CD-SFCRF*

(i) Patient 3 Fully Sampled *(j) Patient 3* L_2 *(k) Patient 3 H*L_0 *(l) Patient 3 CD-SFCRF*

Figure 4.4: Sample T2w results for three patient cases produced using CD-SFCRF, L_2, and HL_0 at 32% radial percentage sampled. Compared to other methods, CD-SFCRF preserves tissue details and contrast especially in the tumourous regions. The arrow shows tumourous region in the fully sampled image (a).

the L_2 and homotopic l_0 minimization reconstruction methods for three cases for T2w images using radial sampling. The L_2 method resulted in blurry images as well as noticeable

radial artifacts at low sampling rates. The HL_0 approach performed better than the L2 minimization and was able to noticeably reduce artifacts and provide a higher quality reconstruction. However, in comparison, the CD-SFCRF was able to better restore details and fine tissue structure in the reconstructed image when compared to HL_0. This is to be expected as the CD-SFCRF takes advantage of more complete data and spatial driven consistencies in a fully connected nature, thus better modeling the underlying tissue detail and structures.

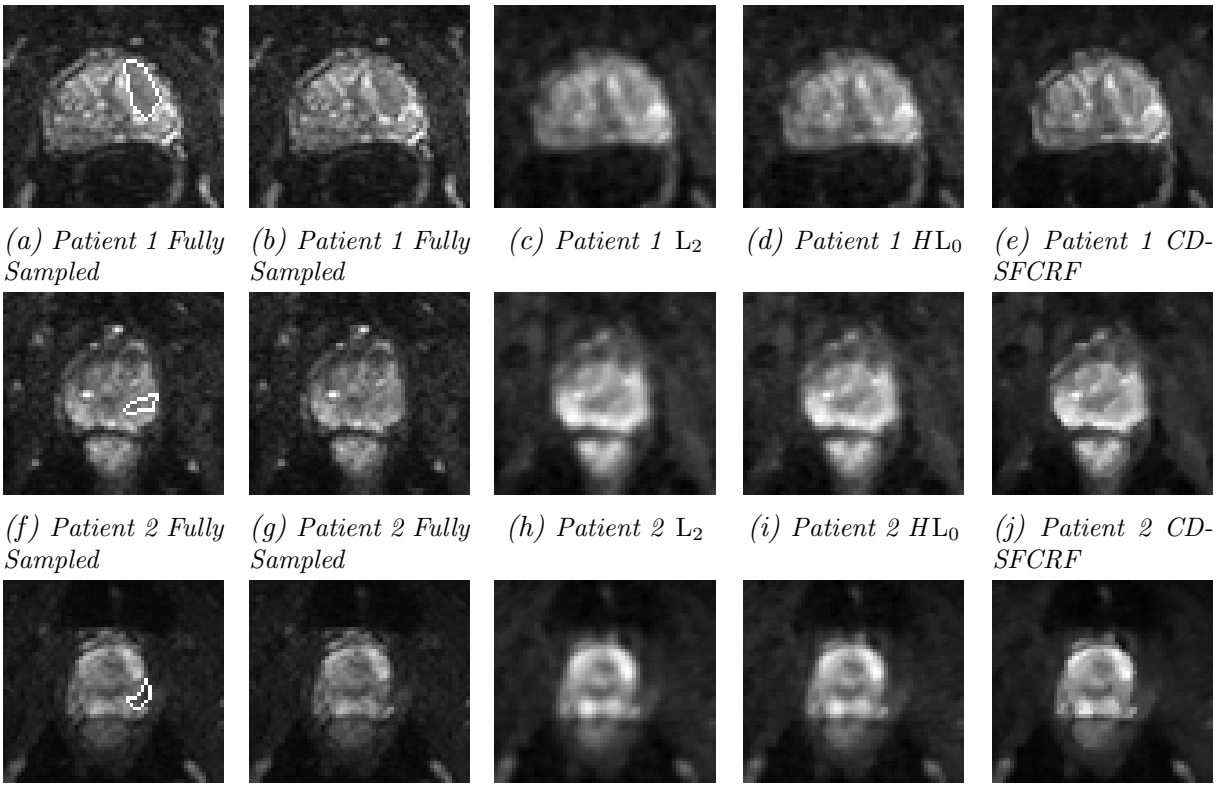

(a) Patient 1 Fully Sampled | *(b) Patient 1 Fully Sampled* | *(c) Patient 1* L_2 | *(d) Patient 1 H*L_0 | *(e) Patient 1 CD-SFCRF*

(f) Patient 2 Fully Sampled | *(g) Patient 2 Fully Sampled* | *(h) Patient 2* L_2 | *(i) Patient 2 H*L_0 | *(j) Patient 2 CD-SFCRF*

(k) Patient 3 Fully Sampled | *(l) Patient 3 Fully Sampled* | *(m) Patient 3* L_2 | *(n) Patient 3 H*L_0 | *(o) Patient 3 CD-SFCRF*

Figure 4.5: Sample DWI results ($b = 100s/mm^2$) for three patient cases produced using CD-SFCRF, L_2, and HL_0 at 32% radial percentage sampled. Compared to other methods, CD-SFCRF preserves tissue details and contrast especially in the tumourous regions. The tumourous region in the fully sampled image is marked (a).

Figures 4.5, 4.6 and 4.7, 4.8 shows the visual comparison between the reconstructed images produced using the proposed CD-SFCRF framework compared with that produced

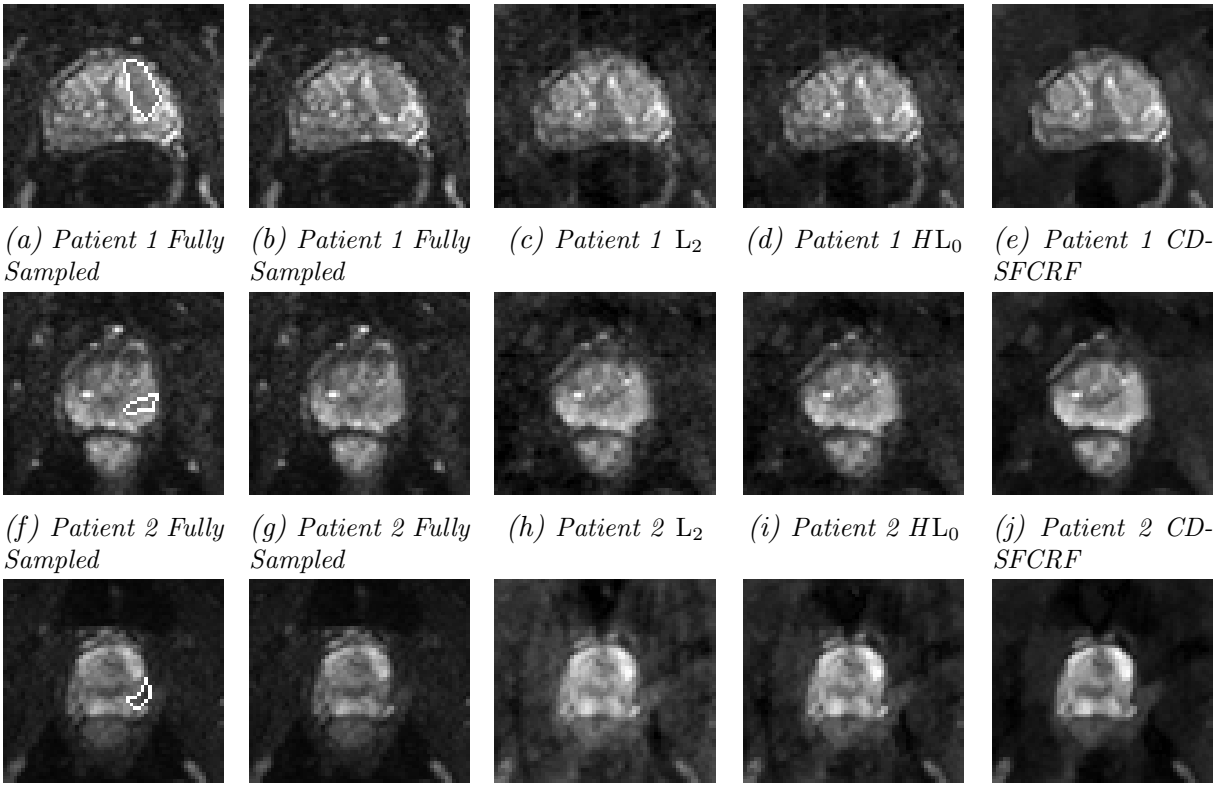

(a) Patient 1 Fully Sampled *(b) Patient 1 Fully Sampled* *(c) Patient 1* L_2 *(d) Patient 1* HL_0 *(e) Patient 1 CD-SFCRF*

(f) Patient 2 Fully Sampled *(g) Patient 2 Fully Sampled* *(h) Patient 2* L_2 *(i) Patient 2* HL_0 *(j) Patient 2 CD-SFCRF*

(k) Patient 3 Fully Sampled *(l) Patient 3 Fully Sampled* *(m) Patient 3* L_2 *(n) Patient 3* HL_0 *(o) Patient 3 CD-SFCRF*

Figure 4.6: Sample DWI results ($b = 100s/mm^2$) for three patient cases produced using CD-SFCRF, L_2, and HL_0 at 32% spiral percentage sampled. Compared to other methods, CD-SFCRF preserves tissue details and contrast especially in the tumourous regions. The tumourous region in the fully sampled image is marked (a).

using the L_2 and HL_0 methods for three patient cases for DWI ($b = 100s/mm^2$) and ADC images for radial and spiral sub-sampling. As it can be seen in both set of figures, the L_2 method resulted in blurry images again with noticeable radial and spiral artifacts. Although the HL_0 approach performed better than the L_2 method, it can be observed once again that the proposed CD-SFCRF approach was able to preserve more fine tissue structure and detail in the reconstructed image when compared to the HL_0 method.

In Figures 4.4 to 4.8, the tumourous regions marked by a radiologist and confirmed by pathology report (biopsy results) are shown by arrow. It can be seen that the proposed CD-SFCRF method preserves the separability of the cancerous and healthy tissue in all

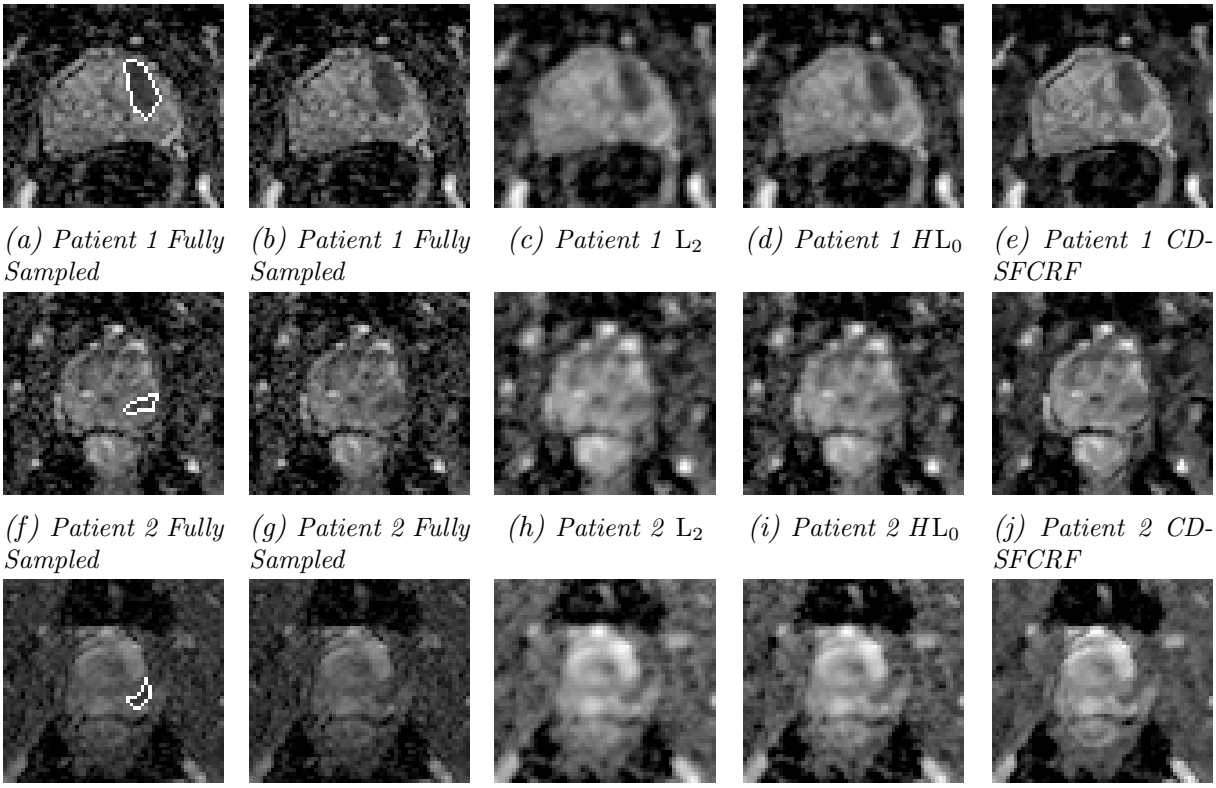

(a) Patient 1 Fully Sampled *(b) Patient 1 Fully Sampled* *(c) Patient 1* L_2 *(d) Patient 1* $H\mathrm{L}_0$ *(e) Patient 1 CD-SFCRF*

(f) Patient 2 Fully Sampled *(g) Patient 2 Fully Sampled* *(h) Patient 2* L_2 *(i) Patient 2* $H\mathrm{L}_0$ *(j) Patient 2 CD-SFCRF*

(k) Patient 3 Fully Sampled *(l) Patient 3 Fully Sampled* *(m) Patient 3* L_2 *(n) Patient 3* $H\mathrm{L}_0$ *(o) Patient 3 CD-SFCRF*

Figure 4.7: Sample ADC map results for three patient cases produced using CD-SFCRF, L_2, and HL_0 at 32% radial percentage sampled. Compared to other methods, CD-SFCRF preserves tissue details and contrast especially in the tumourous regions. The tumourous region in the fully sampled image is marked (a).

cases, which is an important measure for usability of the proposed method in practice. As it can be seen the tumourous regions are blurred in the L_2 method, which may make it difficult to detect for radiologists.

Both quantitative and qualitative analysis demonstrate the potential of the proposed CD-SFCRF framework as a reliable reconstruction approach for compressive sensing in MRI. It demonstrates the ability to produce edge and tissue details at very low sampling rates. The CD-SFCRF framework better utilized available information to produce quality reconstruction given very limited available information. Preservation of tissue structure, detail enhancement and noise and artifact mitigation are very important for MRI as the

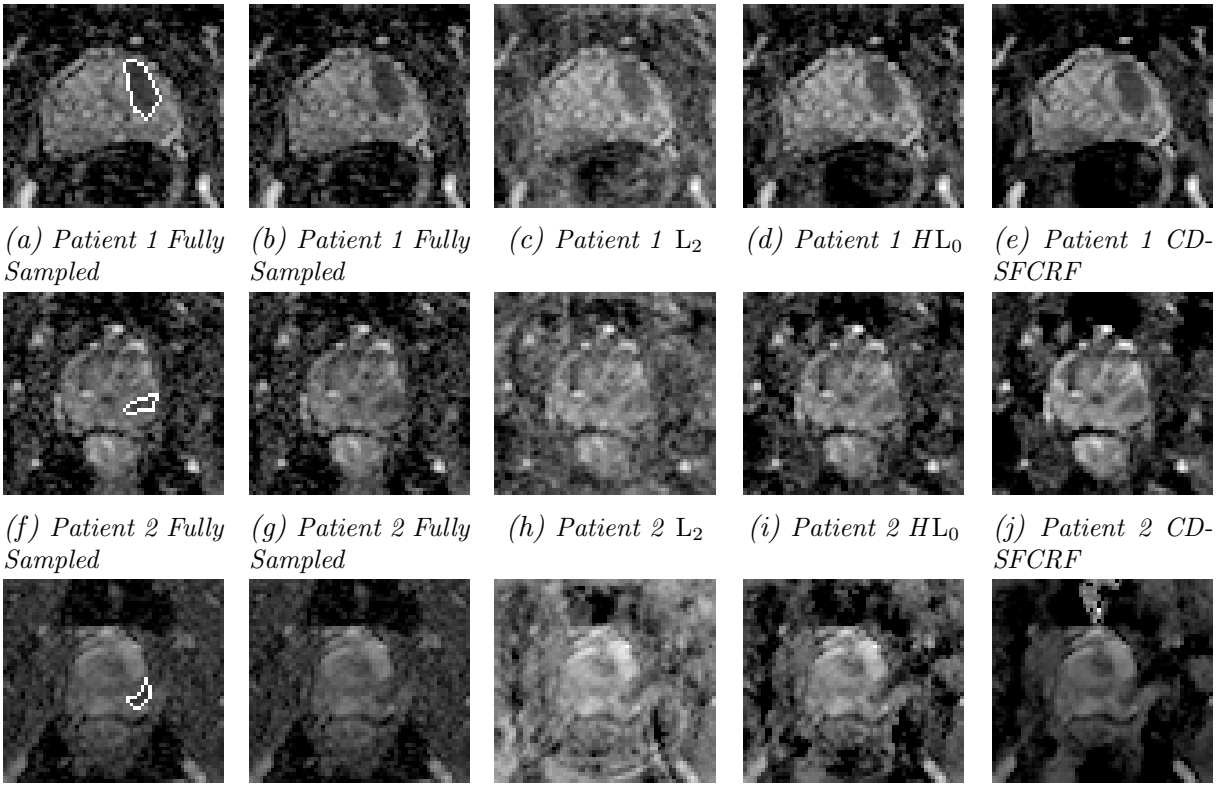

(a) Patient 1 Fully Sampled *(b) Patient 1 Fully Sampled* *(c) Patient 1* L_2 *(d) Patient 1* HL_0 *(e) Patient 1 CD-SFCRF*

(f) Patient 2 Fully Sampled *(g) Patient 2 Fully Sampled* *(h) Patient 2* L_2 *(i) Patient 2* HL_0 *(j) Patient 2 CD-SFCRF*

(k) Patient 3 Fully Sampled *(l) Patient 3 Fully Sampled* *(m) Patient 3* L_2 *(n) Patient 3* HL_0 *(o) Patient 3 CD-SFCRF*

Figure 4.8: Sample ADC map results for three patient cases produced using CD-SFCRF, L_2, and HL_0 at 32% spiral percentage sampled. Compared to other methods, CD-SFCRF preserves tissue details and contrast especially in the tumourous regions. The tumourous region in the fully sampled image is marked (a).

diagnostic quality is directly related to the image quality.

4.2.2 ACD-SFCRF Results

In order to test the ability of the ACD-SFCRF, qualitative and quantitative analysis are performed. The ACD-SFCRF is compared with the original CD-SFCRF [39], as well as classification results based on the four classifiers. The classification masks from the four classifiers are compared with ground truth masks as well to provide a measure of classification accuracy. Quantitative analysis on the include image PSNR analysis, classifier

accuracy analysis, reconstruction timing analysis. Qualitative comparison is only shown for patient 10 slice 14 with b-value 400 for consistency. The single b-value classifier is trained using the b-value 400 images as well.

Classifier Results

Table 4.5: Ten fold classifier accuracy (%)

Fold	single b-value Bayes	multi b-value Bayes	multi b-value ML	Three classifier voting
1	**98.26**	97.89	95.74	97.75
2	**95.44**	94.37	91.44	93.78
3	**95.73**	94.43	91.03	94.01
4	**97.65**	96.85	94.19	96.12
5	**96.57**	95.90	93.90	95.74
6	**96.30**	95.56	91.97	94.54
7	**97.52**	97.17	94.01	96.41
8	**97.64**	96.53	93.78	95.89
9	**97.70**	97.16	94.85	96.23
10	98.37	**98.42**	95.85	97.81
mean	**97.10**	96.41	93.65	95.81

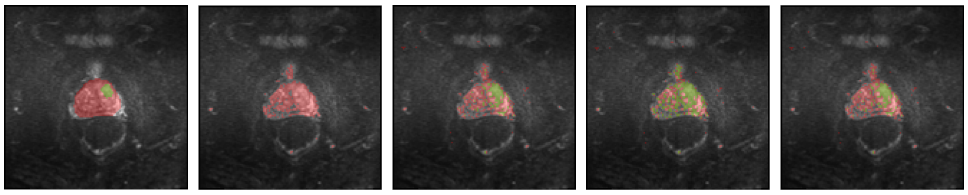

(a) ground truth mask *(b) single b-value Bayes classifier mask* *(c) multi b-value Bayes classifier mask* *(d) multi b-value ML classifier mask* *(e) combined classifier mask*

Figure 4.9: Comparison of different classification masks for prostate(red) and tumor(green)

The accuracy of each classifier is tested by comparing the number of correct classification in each of the masks generated with ground truth masks. Table 4.5 shows the accuracy of each classifier through ten fold cross validation classifier testing. The single class modified Bayes classifier performed the best in classifying each pixel at 97% overall accuracy. This is because the single b-value Bayes classifier is trained specifically on images with similar b-values, therefore tissue structures will have the similar pixel values for the same b-value. The multi b-value Bayes classifier came in second with overall 96% accuracy. The multi b-value ML classifier had the least accuracy with 94% overall, as the class probabilities did not favor any single class, therefore the classifier could not use additional information to guide the classification. The three class voting classifier performed a good job of classification as well with 96% accuracy, it was able to combine the results of all three classifiers.

Table 4.6: Ten fold reconstruction PSNR (db)

Fold	CD-SFCRF	ACD-SFCRF (ground truth mask)	ACD-SFCRF (single b-value MAP)	ACD-SFCRF (multi b-value MAP)	ACD-SFCRF (multi b-value ML)	ACD-SFCRF (three classifier voting)
1	37.74	37.57	37.54	37.55	37.55	37.55
2	37.95	37.83	37.83	37.83	37.83	37.84
3	38.38	38.12	38.13	38.12	38.13	38.13
4	37.45	37.20	37.20	37.20	37.27	37.22
5	37.85	37.67	37.71	37.61	37.63	37.65
6	38.22	38.04	38.03	38.08	38.06	38.03
7	38.22	37.83	37.79	37.85	37.84	37.83
8	38.76	38.69	38.70	38.70	38.63	38.68
9	39.89	39.62	39.63	39.62	39.62	39.63
10	38.34	38.20	38.18	38.18	38.13	38.20
mean	38.27	38.07	38.07	38.07	38.06	38.07

Visual classification results can be seen in Figure 4.9, the single b-value Bayes classifier classified most of the prostate correctly. However, it did not classify any pixels as tumor which is incorrect. The accuracy of the classifier is still very high because the difference between the ground truth is only a few pixels. The multi b-value Bayes classifier did a better job of classifying tumor pixels in addition to the prostate that was classified. This

Table 4.7: Ten fold reconstruction run time for 30 iterations (seconds)

Fold	CD-SFCRF	ACD-SFCRF (ground truth mask)	ACD-SFCRF (single b-value MAP)	ACD-SFCRF (multi b-value MAP)	ACD-SFCRF (multi b-value ML)	ACD-SFCRF (three classifier voting)
1	15.71	14.54	14.47	14.52	14.55	14.47
2	14.82	14.11	14.01	14.03	14.17	14.03
3	14.80	14.02	13.96	13.96	14.01	13.99
4	14.38	13.37	13.38	13.57	13.33	13.55
5	15.69	14.22	14.22	14.14	14.27	14.15
6	15.80	14.55	14.75	14.66	14.48	14.56
7	16.09	14.72	15.27	14.65	14.94	14.84
8	18.79	17.48	17.66	17.43	17.52	17.45
9	17.95	16.84	16.78	16.74	16.62	16.83
10	16.49	15.54	15.72	15.77	15.74	15.62
mean	16.02	14.91	14.99	14.92	14.94	14.92

is because the multi-b value classifier utilizes more complete information in regards to tumors attributes. The ML classifier over classified on the number of tumor pixels there are and this lowered the accuracy of the classifier compared to the other classifiers. Finally, the combined classifier did a good job to capture the tumor area while at the same time capturing the outline of the prostate. The combined classifier in the end looks very similar to the multi b-value Bayes classifier. This is reflected from the accuracy table in Table 4.5 as well.

From both visual and quantitative results, we can see that the multi b-value Bayes classifier is a reliable classifier for classifying regions of interest while maintaining good accuracy to ground truth data.

Image Reconstruction Results

The PSNR analysis is performed between the CD-SFCRF, ACD-SFCRF with ground truth and ACD-SFCRF with each of the classified tumor and prostate masks in comparison to the original image. Table 4.6 shows the comparisons between the methods. The ACD-SFCRF had a average decrease of $0.2dB$ in comparison to the CD-SFCRF. This is expected as the

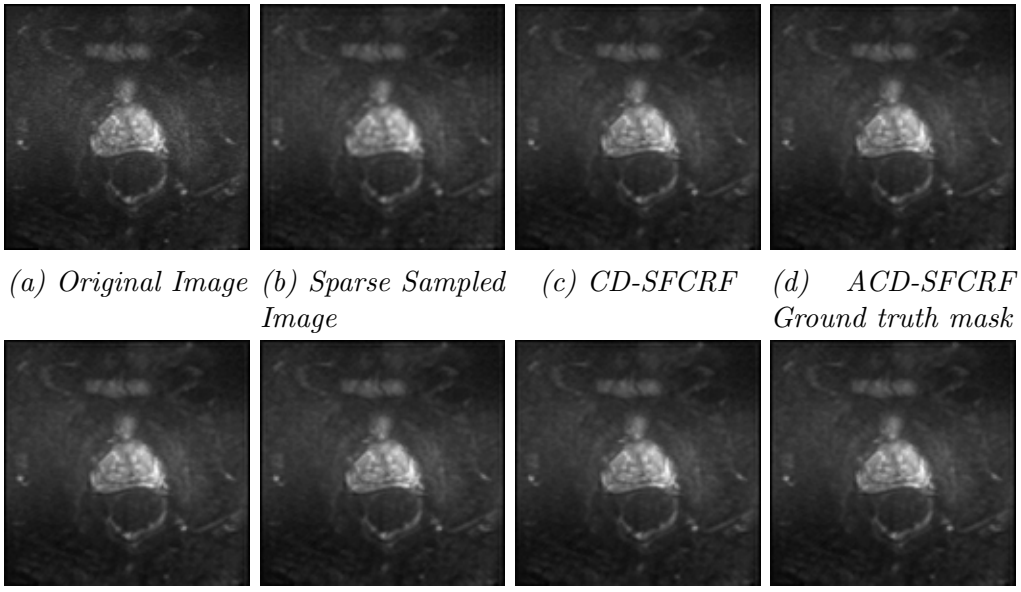

(a) Original Image *(b) Sparse Sampled Image* *(c) CD-SFCRF* *(d) ACD-SFCRF Ground truth mask*

(e) ACD-SFCRF single b-value Bayes mask *(f) ACD-SFCRF multi b-value Bayes mask* *(g) ACD-SFCRF multi b-value ML mask* *(h) ACD-SFCRF combined classifier mask*

Figure 4.10: Comparison of different reconstruction results

ACD-SFCRF uses a smaller neighborhood connectivity in areas of irrelevance compared to the neighborhood connectivity constant of 80% used for the CD-SFCRF. There is little difference between the different classifiers as the majority of the image are areas of non relevance. The ACD-SFCRF can increase the PSNR in regions of interest while lowering the computation complexity in areas of irrelevance. This effect can be seen in Table 4.7 as over 30 iterations the ACD-SFCRF is faster than the CD-SFCRF by more than one second. This shows the ability of the ACD-SFCRF to process areas of irrelevance more efficiently with minor decrease in image quality. Considering the CD-SFCRF itself is a very powerful reconstruction algorithm already. The ACD-SFCRF performed a good job in segmenting the image and adapting the CD-SFCRF for better efficiency in areas of irrelevance while maintaining high image quality for regions of interest.

Visually, comparison between the CD-SFCRF and ACD-SFCRF using different classifiers is demonstrated in Figure 4.10. The ACD-SFCRF produced similar level of reconstruction to the CD-SFCRF. The ACD-SFCRF was able to restore details and fine tissue structure in the reconstruction. This is to be expected as the ACD-SFCRF takes advantage of more complete neighborhood consistencies in a fully connected nature. The model

takes into account edge and other details when performing inference. The ACD-SFCRF adapted the reconstruction to enhance details in regions of interest while increasing the efficiency in areas of irrelevance without losing image quality. This utilization of training data and the segmentation of the image allowed the ACD-SFCRF to take advantage of the advanced reconstruction of the CD-SFCRF while increasing reconstruction efficiency and improving on overall image quality.

Both qualitative and quantitative analysis demonstrate the potential of the ACD-SFCRF as a reliable reconstruction approach for compressive sensing in MRI. The ACD-SFCRF has the ability to produce edge and tissue details at low sampling rates, by fully utilizing available information while increasing overall efficiency and improving image quality. Preservation of tissue structure, detail enhancement and noise reduction are very important for MRI as the diagnostic quality is directly related to the image quality.

4.2.3 CCD-SFCRF Results

Table 4.8: Calculated PSNR for different methods

Sampling Percentage (%)	$PSNR_{TV}(dB)$	$PSNR_{CD-SFCRF}(dB)$	$PSNR_{CCD-SFCRF}(dB)$
5	26.30	27.58	27.69
10	31.06	35.16	29.54
15	34.64	37.84	30.37
19	36.42	39.10	30.86
24	37.59	40.06	30.90
28	39.05	41.20	29.67
32	41.03	41.90	27.87
36	42.07	42.70	27.36

To evaluate the quality of reconstruction of the proposed compensated cross domain stochastically fully connected conditional random field (CCD-SFCRF) method, comparisons are made between the total variation [18, 24, 25] reconstruction as well as the CD-SFCRF [39] from previous work. These methods are compared quantitatively though PSNR analysis and visually. Because current MRI acquisitions are already sub-sampled in current systems, PSNR would not be a good measure to compare reconstructed results to already sparsely sampled original images. Therefore, PSNR analysis is performed on fully sampled phantom MRI images. Reconstruction results from the CCD-SFCRF on phantom

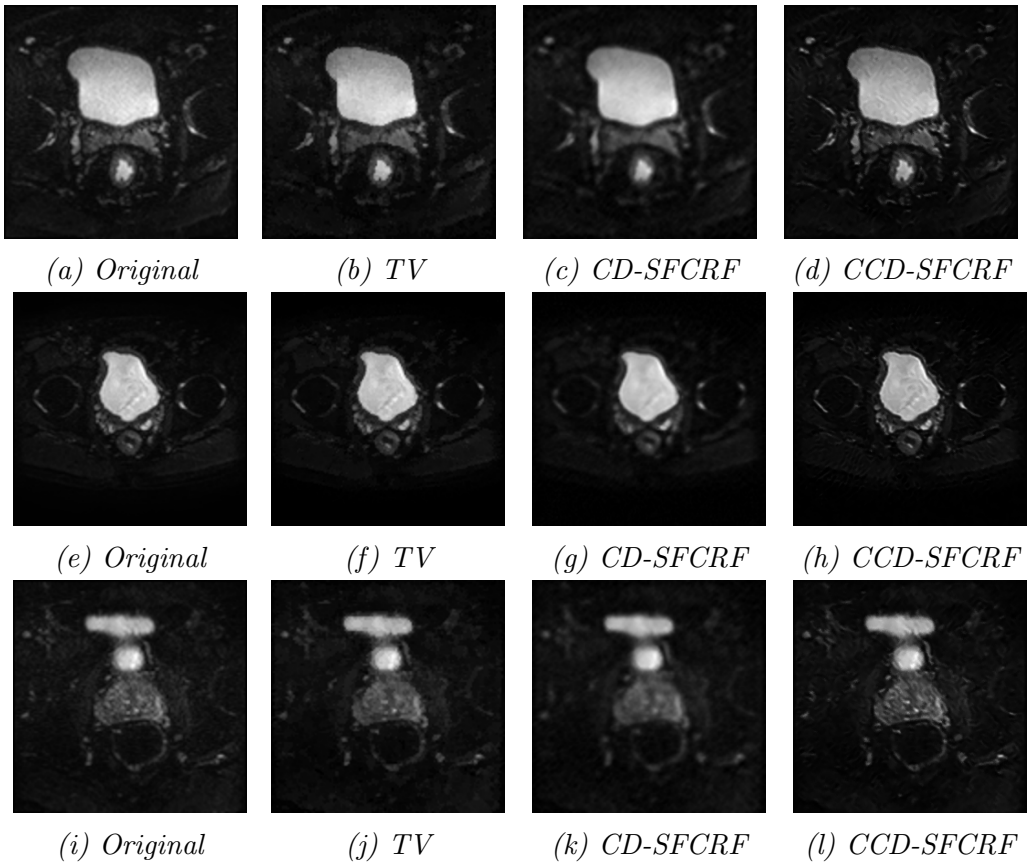

(a) Original *(b) TV* *(c) CD-SFCRF* *(d) CCD-SFCRF*

(e) Original *(f) TV* *(g) CD-SFCRF* *(h) CCD-SFCRF*

(i) Original *(j) TV* *(k) CD-SFCRF* *(l) CCD-SFCRF*

Figure 4.11: Visual result of proposed reconstruction method (CCD-SFCRF) for patient 1 to 3, compared to existing methodology (TV, CD-SFCRF) at 32% percentage sampled

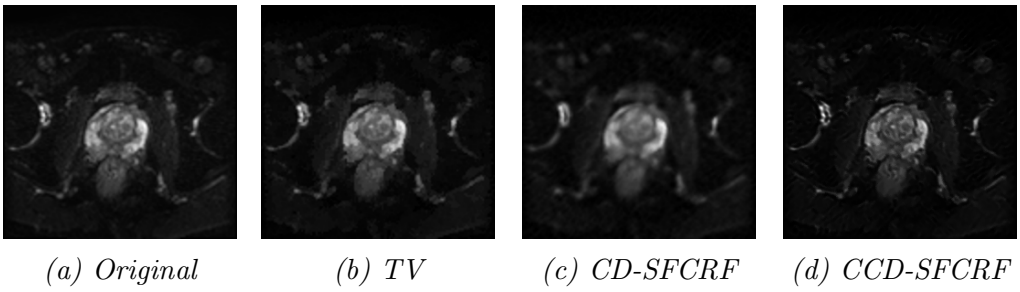

(a) Original *(b) TV* *(c) CD-SFCRF* *(d) CCD-SFCRF*

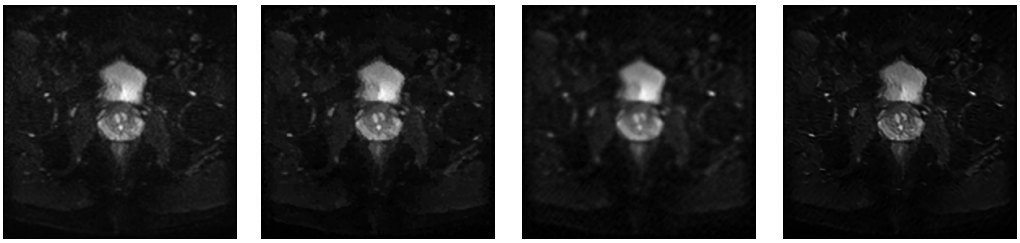

(e) Original *(f) TV* *(g) CD-SFCRF* *(h) CCD-SFCRF*

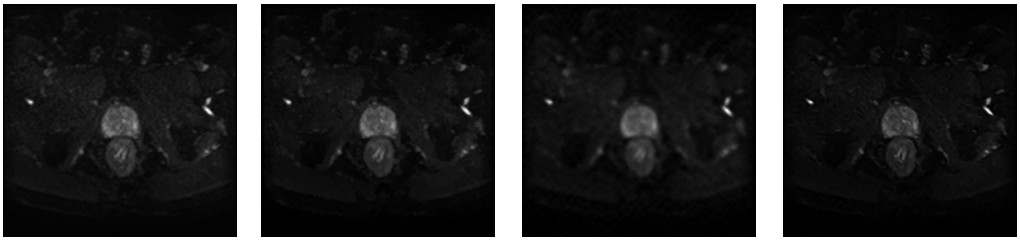

(i) Original *(j) TV* *(k) CD-SFCRF* *(l) CCD-SFCRF*

Figure 4.12: Visual result of proposed reconstruction method (CCD-SFCRF) for patient 4 to 6, compared to existing methodology (TV, CD-SFCRF) at 32% percentage sampled

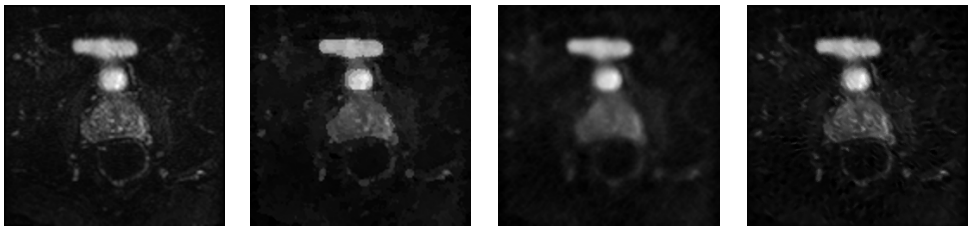

(a) 15% *Original*

(b) 15% *TV*

(c) 15% *CD-SFCRF*

(d) 15% *CCD-SFCRF*

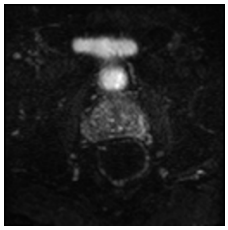

(e) 20% *Original*

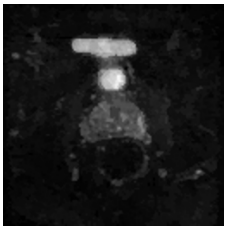

(f) 20% *TV*

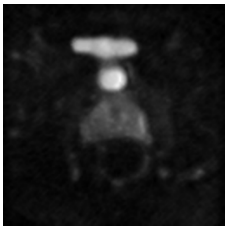

(g) 20% *CD-SFCRF*

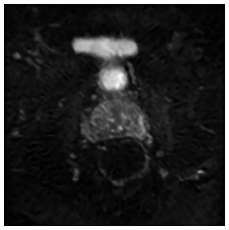

(h) 20% *CCD-SFCRF*

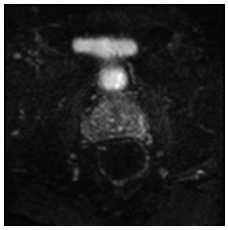

(i) 24% *Original*

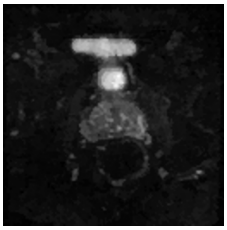

(j) 24% *TV*

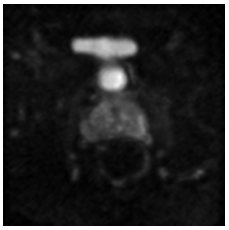

(k) 24% *CD-SFCRF*

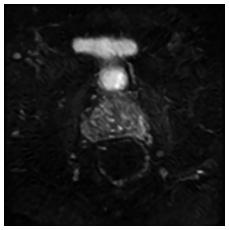

(l) 24% *CCD-SFCRF*

Figure 4.13: Visual result of proposed reconstruction method (CCD-SFCRF) compared to existing methodology (TV,CD-SFCRF) at different $(15\%, 19\%, 24\%)$ percentage sampled for patient 4

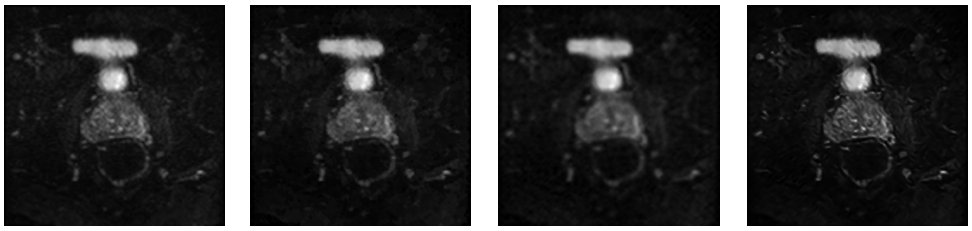

(a) 32% *Original* *(b)* 32% *TV* *(c)* 32% *CD-SFCRF* *(d)* 32% *CCD-SFCRF*

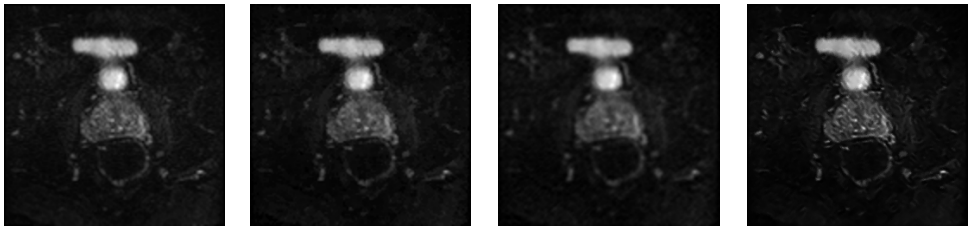

(e) 36% *Original* *(f)* 36% *TV* *(g)* 36% *CD-SFCRF* *(h)* 36% *CCD-SFCRF*

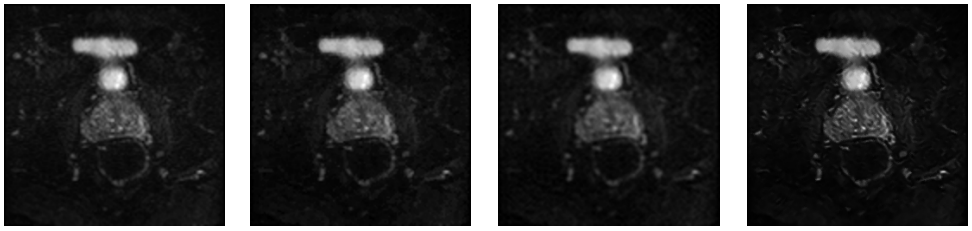

(i) 40% *Original* *(j)* 40% *TV* *(k)* 40% *CD-SFCRF* *(l)* 40% *CCD-SFCRF*

Figure 4.14: Visual result of proposed reconstruction method (CCD-SFCRF) compared to existing methodology (TV,CD-SFCRF) at different $(32\%, 36\%, 40\%)$ percentage sampled for patient 4

MRI images can be quantitatively measured. Qualitative comparisons can be observed from reconstructing sparsely sampled slices from six different patients using the proposed CCD-SFCRF.

Figure 4.15 shows PSNR trends calculated for the different methods, the PSNR values are evaluated according to the original fully sampled high-resolution phantom MRI data. Comparisons show that at the lowest sampling rate the PSNR for the CCD-SFCRF was better than the other methods. However, as the sampling rate increases, the PSNR for the CCD-SFCRF drops significantly, this is because the PSNR calculation for the CCD-SFCRF was performed on a resized version of the original image and this can potentially throw off PSNR calculations. The resizing is required for the compensation and this makes PSNR an unreliable comparison for this study. Furthermore, as the amount of available information increases, the reconstruction results are much better than the original image as the original image contains degredations and artifacts. This affects PSNR calculations. Visually the phenomenon described above can be observed.

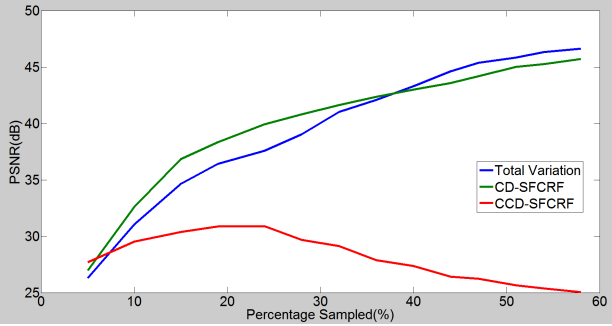

Figure 4.15: PSNR trends for different sampling rates.

Figures 4.16, 4.17 shows the visual comparison between the proposed CCD-SFCRF compared to the other iterative methods for different sparse sampling ratios on the phantom image. The CCD-SFCRF was able to produce high quality reconstruction by fully utilizing available information especially at higher sampling percentages. At higher sampling percentages, because of the vast amount of available information, the results between TV, CD-SFCRF and CCD-SFCRF are very similar and less differentiated. At low sampling rates because there are a very high amount of artifacts as any deblurring can produce artifacts and this is evident as for the low sampling percentages, the TV and CD-SFCRF reconstruction has better visual results due to the smoothing. However, at higher sampling percentages the CCD-SFCRF builds on the good reconstruction result from the CD-SFCRF reconstruction to produce images with high detail and structure preservation.

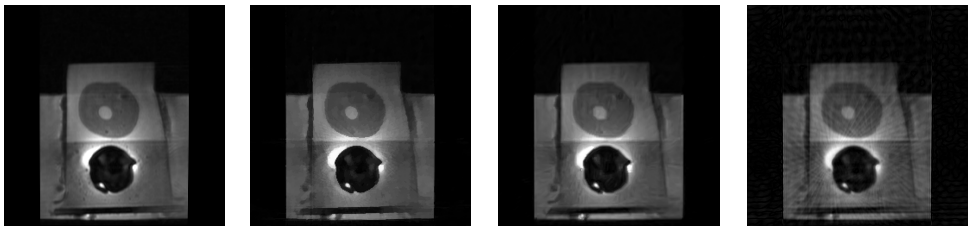

(a) 15% *Original* *(b)* 15% *TV* *(c)* 15% *CD-SFCRF* *(d)* 15% *CCD-SFCRF*

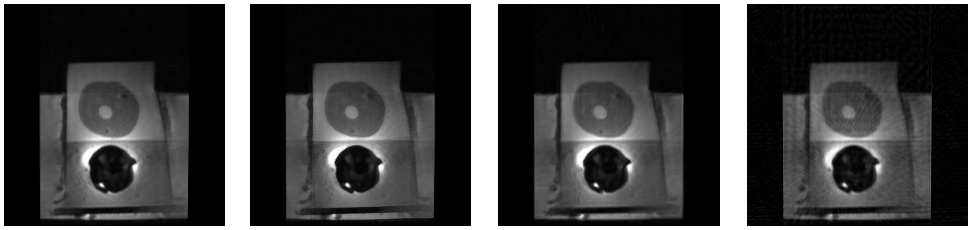

(e) 20% *Original* *(f)* 20% *TV* *(g)* 20% *CD-SFCRF* *(h)* 20% *CCD-SFCRF*

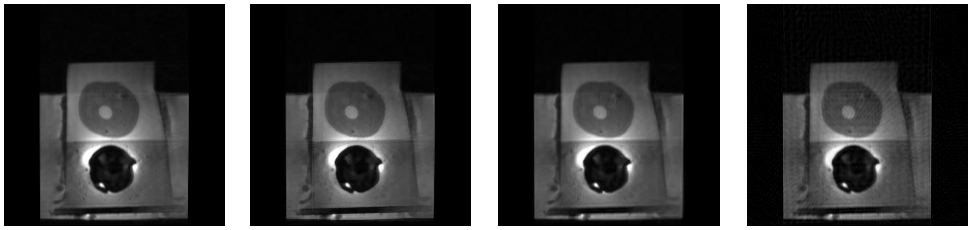

(i) 24% *Original* *(j)* 24% *TV* *(k)* 24% *CD-SFCRF* *(l)* 24% *CCD-SFCRF*

Figure 4.16: Visual result of proposed reconstruction method (CCD-SFCRF) compared to existing methodology (TV,CD-SFCRF) at different $(15\%, 19\%, 24\%)$ percentage sampled for phantom data.

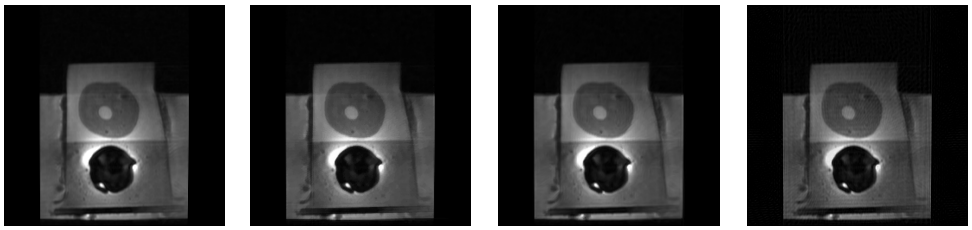

(a) 32% *Original* *(b)* 32% *TV* *(c)* 32% *CD-SFCRF* *(d)* 32% *CCD-SFCRF*

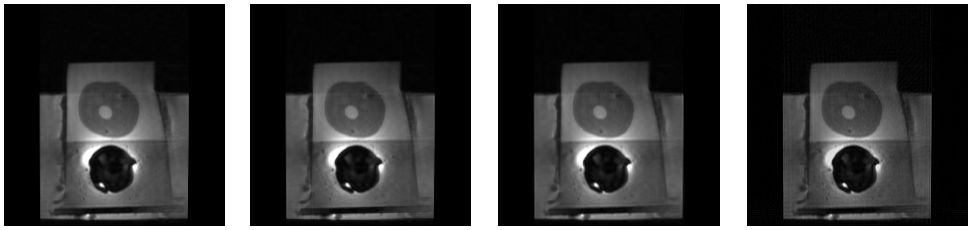

(e) 36% *Original* *(f)* 36% *TV* *(g)* 36% *CD-SFCRF* *(h)* 36% *CCD-SFCRF*

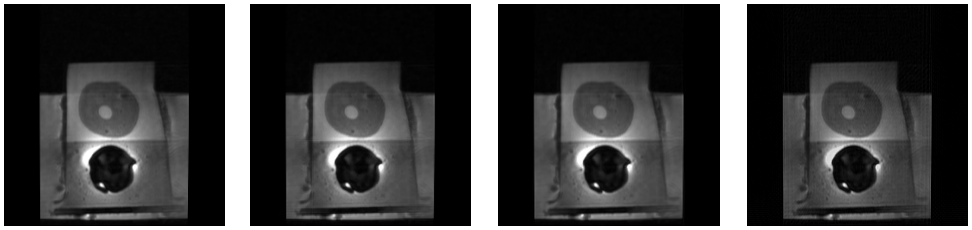

(i) 40% *Original* *(j)* 40% *TV* *(k)* 40% *CD-SFCRF* *(l)* 40% *CCD-SFCRF*

Figure 4.17: Visual result of proposed reconstruction method (CCD-SFCRF) compared to existing methodology (TV,CD-SFCRF) at different (32%, 36%40%) percentage sampled for phantom data.

Figures 4.11, 4.12 shows the visual comparison between the proposed CCD-SFCRF compared to the other iterative image reconstruction techniques for slices in six patients. TV reconstruction produces block like regions within the image, this is to be expected as the total variation constraint promotes regional smoothness. The CD-SFCRF was able to eliminate the radial artifacts from the sparse sampling process. Furthermore, there was blurring as a result of the artifact elimination and from originally introduced blurring from sparse sampling. The CCD-SFCRF was able to preserve edges and structural details while eliminating blurring and reducing artifacts. Comparing with the original fully sampled image, it is visible that the CCD-SFCRF restored a lot of the edge details while effectively eliminating blur from the original image. The CCD-SFCRF is a great addition to the CD-SFCRF as the CD-SFCRF was able to greatly eliminate the sparse sampling artifacts at the cost of image sharpness and edge distinction.

Figure 4.13, 4.14 shows the visual comparison between the proposed CCD-SFCRF compared to the other iterative methods for different sparse sampling ratios on the same slice in patient 4. At low sampling percentages, total variation reconstruction produced good reconstruction with blocking artifacts as expected. The CD-SFCRF efficiently eliminated artifacts at the cost of a significantly blurred image. The CCD-SFCRF was able to produce high quality reconstruction and good tissue differentiation. Given the sparsity of available information, the CCD-SFCRF at 15% sub sampling was able to restore a significant amount of details comparable to the original fully sampled image. At higher sampling rates, with an increased amount of available information the CCD-SFCRF was able to further produce increased tissue and structural details comparable even surpassing the original images. The total variation reconstruction results does not increase significantly as the sampling rate increases. This is the limitation of the total variation reconstruction. The CD-SFCRF have better reconstruction and tissue details as the sampling rate increases, the amount of tissue and structure details increases while the artifacts are consistently eliminated throughout the different sampling rates. The CCD-SFCRF based on the CD-SFCRF was able to take advantage of the scalability of the CD-SFCRF to produce even better reconstruction results.

Quantitatively, the CCD-SFCRF does not edge out the other methodologies in the PSNR calculations. Qualitatively, the CCD-SFCRF demonstrates a very high scalability with increasing amount of available information. Furthermore, at low resolutions the CCD-SFCRF produced very viable reconstruction results with very little available information. This demonstrates the superior reconstruction ability of the CCD-SFCRF to produce high quality reconstruction given any amount of available data. The visual results demonstrate the potential of the CCD-SFCRF to be a viable reconstruction algorithm for compressive sensing MRI.

4.3 Chapter Summary

In this chapter, both qualitative and quantitative comparisons using real patient data were made for the CD-SFCRF and its extension frameworks with existing state of the art methods. Results demonstrated the ability of the CD-SFCRF to utilizes original k-space measurements with spatial domain pairwise potentials to reconstruct compressive sensing MRI data with high visual fidelity. Furthermore, the ACD-SFCRF improves the algorithm efficiency by being selective in the amount of pairwise calculations made based on the data presented. Results demonstrate a comparable reconstruction result to the CD-SFCRF while being faster in runtime. Additionally, the CCD-SFCRF was able to further improve the reconstruction of the CD-SFCRF by introducing a compensation step. This effectively removes image degradations caused by the imaging apparatus to produce further enhanced tissue and structural details. These results demonstrate the ability of the CD-SFCRF as a viable reconstruction framework for compressive sensing MRI.

Chapter 5

Summary and Future Work

5.1 Summary

Magnetic resonance imagery (MRI) is a non-invasive and crucial imaging modality for the early detection of prostate cancer, one of the four major types of cancer affecting North Americans. MRI provides multi-modal information that can be used for accurately detecting tumor regions to guide the diagnosis for medical staff. However, our reliance on MRI is severely hindered by the long acquisition times associated with MRI imaging. Compressive sensing demonstrates the potential to reduce acquisition times by sparsely sampling a sufficient set of observations. Compressive sensing strategies are usually accompanied by strong reconstruction algorithms to facilitate for compressive sensing MRI. Current reconstruction algorithms are usually focused in a singular domain and cannot fully take advantage of the MRI original observations that are made in the k-space.

Chapter 3 introduced a cross domain stochastically fully connected conditional random field (CD-SFCRF) approach for the reconstruction of compressive sensing MRI data by utilizing both original k-space measurements as well as neighborhood consistencies in the spatial domain. Chapter 3 described the underlying mathematics behind the framework and the implementation details associated with this new approach. Additionally, extension frameworks are introduced and mathematiclaly formulated as well. The first extension being an adaptive CD-SFCRF (ACD-SFCRF) approach that optimizes the CD-SFCRF algorithm by learning and classifying the imagery before hand to increases the focus on regions of interest to enhance image quality and structural details while lowering focus in regions of non interest to increase algorithm processing speed. Secondly, a compensated CD-SFCRF (CCD-SFCRF) is introduced that learns the MRI imaging apparatus proper-

ties and compensates for the degradations caused by the imaging system. By performing compensation image quality and tissue details can be further enhanced.

Chapter 4 explains the experimental procedure partaken to evaluate the performance of the CD-SFCRF and its extension frameworks. Real patient data with tumor and prostate segmentation regions are used. Different evaluation criteria are explained and simulation parameters identified. Experimental results demonstrate the ability of the CD-SFCRF to utilize additional information for higher reconstruction quality. The CD-SFCRF was able to further lower the amount of available information while maintaining image fidelity and accurate tissue detail. Additionally, the ACD-SFCRF was able to produced similar results to the CD-SFCRF while lowering processing time and increasing efficiency. Finally, the CCD-SFCRF demonstrated the ability to further enhance image details and structural information at low sampling rates. Experimental results demonstrates the CD-SFCRF and its associated extensions as viable reconstruction algorithms to facilitate for compressive sensing MRI used in the early diagnosis of prostate cancer.

5.2 Recommendations

5.3 Future Work

Although initial results of the CD-SFCRF are promising, there are additional work that can be done to improve the framework and the reconstruction result.

5.3.1 Computer Aided Diagnosis Applications

Compressive sensing method used to reconstruct MR image can influence the performance of the computer-aided diagnosis (CAD) tools. For example, several radiomics-based CAD algorithms have been proposed for automatic prostate cancer detection which use T2w and DWI to extract texture and morphological features fed into a classifier [40–45]. These algorithms heavily rely on the quality of regions of interests in similar cases in DWI and therefore, it is expected that a reconstructed MRI with better quality will improve the performance. As future work, we will investigate the effect of the proposed compressive sensing method on the detection accuracies of these radiomics-based CAD algorithms with respect to the L_2 and HL_0 methods. Moreover, recently, computational diffusion MRI (CD-MRI) has been introduced which utilizes the wealth of information in DW-MRI to computationally construct new sequences of MRI that potentially will help radiologists with

more accurate and consistent diagnosis [7, 46]. The proposed CD-SFCRF framework will be integrated into CD-MRI algorithms [7, 46] to investigate whether CD-SFCRF improves the separability of cancerous and healthy tissues in prostate for these computationally generated MR sequences with respect to the L_2 and HL_0 methods.

5.3.2 Region Specific Compressive *k*-space Sampling

Different types of body organs and body types have been shown to be sparse in different domains [13]. This means that for different MRI imagery the sparseness of the sampling as well as the location in the k-space that is sampled can be trained to better utilize this information. By exploring the different type of sparse sampling to use for different tissue types , it is possible to reduce sampling percentages to only sample the necessary information for the specific organ/area of interest.

5.3.3 Advanced Classifier Integration to ACD-SFCRF

The ACD-SFCRF demonstrated that for by segmenting regions of interest it is possible to preserve the image fidelity in regions of interest while improving on the processing time of the overall algorithm. The classifier used in this experiment was very basic and simple. Using a more accurate classifier could greatly increase the quality of the segmentation of the area of interest. If the segmentation quality is very good, then the amount of neighborhood connections for areas of non interest can be greatly decreased and the efficiency can be greatly increased. Furthermore, the amount of details in the areas of interested can be enhanced as well by increasing the stochastic connections.

5.3.4 Compensated Adaptive CD-SFCRF

Individually the ACD-SFCRF, the CCD-SFCRF has demonstrated their benefits and capabilities. one future work could be to combine the two frameworks together, with the ACD-SFCRF improving the efficiency while the CCD-SFCRF applying compensation. This combined framework have the potential to greatly increase image quality with faster algorithm processing speed.

References

[1] Canadian Cancer Society's Advisory Committee on Cancer Statistics, "Canadian cancer statistics 2015," Canadian Cancer Society, cancer.ca/statistics., Tech. Rep. 1, 5 2015.

[2] American Cancer Society, "American Cancer Society. Cancer Facts and Figures 2015. Atlanta: American Cancer Society; 2015." American Cancer Society, http://www.cancer.org/research/cancerfactsstatistics/cancerfactsfigures2015/, Tech. Rep. 1, 5 2015.

[3] A. Bradford, "Prostate Cancer: Symptoms, Diagnosis and Treatments," *livescience.com*, April 2015, (Accessed on 03/10/2016).

[4] Prostate Cancer Canada, "Prostate cancer - prostate cancer canada," (Accessed on 03/10/2016).

[5] American Cancer Society, "Prostate Cancer Prevention and Early Detection," http://www.cancer.org/acs/groups/cid/documents/webcontent/003182-pdf.pdf, (Accessed on 04/21/2016).

[6] A. Berger, "How does it work?: Magnetic resonance imaging," *BMJ: British Medical Journal*, vol. 324, no. 7328, p. 35, 2002.

[7] A. Wong, J. Glaister, A. Cameron, and M. Haider, "Correlated diffusion imaging," *BMC Medical Imaging*, vol. 13, no. 1, p. 26, 2013. [Online]. Available: http://www.biomedcentral.com/1471-2342/13/26

[8] M. A. Jacobs, T. S. Ibrahim, and R. Ouwerkerk, "MR Imaging: Brief Overview and Emerging Applications 1," *Radiographics*, vol. 27, no. 4, pp. 1213–1229, 2007.

[9] W. A. Edelstein, M. Mahesh, and J. A. Carrino, "MRI: Time Is Doseand Money and Versatility," *Journal of the American College of Radiology: JACR*, vol. 7, no. 8, p. 650, 2010.

[10] R. Baraniuk, "Compressive Sensing," *IEEE Signal Processing Magazine*, vol. 24, no. July, pp. 1–9, 2007.

[11] E. J. Candès, "Compressive sampling," *Int. Congress of Mathematics,*, vol. 3, pp. 1433–1452, 2006.

[12] D. Donoho, "Compressed sensing," *IEEE Transactions on Information Theory*, vol. 52, no. 4, pp. 1289–1306, Apr. 2006. [Online]. Available: http://ieeexplore.ieee.org/lpdocs/epic03/wrapper.htm?arnumber=1614066

[13] M. Lustig, D. Donoho, and J. M. Pauly, "Sparse MRI: The application of compressed sensing for rapid MR imaging." *Magnetic resonance in medicine : official journal of the Society of Magnetic Resonance in Medicine / Society of Magnetic Resonance in Medicine*, vol. 58, no. 6, pp. 1182–95, Dec. 2007. [Online]. Available: http://www.ncbi.nlm.nih.gov/pubmed/17969013

[14] D. Liang, B. Liu, J. Wang, and L. Ying, "Accelerating SENSE using compressed sensing." *Magnetic resonance in medicine : official journal of the Society of Magnetic Resonance in Medicine / Society of Magnetic Resonance in Medicine*, vol. 62, no. 6, pp. 1574–84, Dec. 2009. [Online]. Available: http://www.ncbi.nlm.nih.gov/pubmed/19785017

[15] J. C. Ye, S. Tak, Y. Han, and H. W. Park, "Projection reconstruction MR imaging using FOCUSS." *Magnetic resonance in medicine : official journal of the Society of Magnetic Resonance in Medicine / Society of Magnetic Resonance in Medicine*, vol. 57, no. 4, pp. 764–775, Apr. 2007. [Online]. Available: http://www.ncbi.nlm.nih.gov/pubmed/17390360

[16] A. Wong, A. Mishra, P. Fieguth, and D. a. Clausi, "Sparse reconstruction of breast MRI using homotopic L0 minimization in a regional sparsified domain." *IEEE transactions on bio-medical engineering*, vol. 60, no. 3, pp. 743–52, Mar. 2013. [Online]. Available: http://www.ncbi.nlm.nih.gov/pubmed/23512112

[17] X. Qu, X. Cao, D. Guo, C. Hu, and Z. Chen, "Compressed Sensing MRI with Combined Sparsifying transforms and Smooted L0 Norm Minimization," in *ICASSP 2010*, 2010, pp. 626–629.

[18] K. T. Block, M. Uecker, and J. Frahm, "Undersampled radial MRI with multiple coils. Iterative image reconstruction using a total variation constraint." *Magnetic resonance in medicine : official journal of the Society of Magnetic Resonance in Medicine / Society of Magnetic Resonance in Medicine*, vol. 57, no. 6, pp. 1086–98, Jun. 2007. [Online]. Available: http://www.ncbi.nlm.nih.gov/pubmed/17534903

[19] J. Trzasko and A. Manduca, "Highly undersampled magnetic resonance image reconstruction via homotopic-minimization," *Medical imaging, iEEE Transactions on*, vol. 28, no. 1, pp. 106–121, 2009.

[20] R. Chartrand, "Fast algorithms for nonconvex compressive sensing: Mri reconstruction from very few data," in *Biomedical Imaging: From Nano to Macro, 2009. ISBI'09. IEEE International Symposium on*. IEEE, 2009, pp. 262–265.

[21] W. Yin, S. Osher, D. Goldfarb, and J. Darbon, "Bregman iterative algorithms for l_1-minimization with applications to compressed sensing," *SIAM Journal on Imaging Sciences*, vol. 1, no. 1, pp. 143–168, 2008.

[22] M. A. Figueiredo, R. D. Nowak, and S. J. Wright, "Gradient projection for sparse reconstruction: Application to compressed sensing and other inverse problems," *Selected Topics in Signal Processing, IEEE Journal of*, vol. 1, no. 4, pp. 586–597, 2007.

[23] T. Goldstein and S. Osher, "The split Bregman method for L1-regularized problems," *SIAM Journal on Imaging Sciences*, vol. 2, no. 2, pp. 323–343, 2009.

[24] Y. Wang, J. Yang, W. Yin, and Y. Zhang, "A new alternating minimization algorithm for total variation image reconstruction," *SIAM Journal on Imaging Sciences*, vol. 1, no. 3, pp. 248–272, 2008.

[25] S. Osher, M. Burger, D. Goldfarb, J. Xu, and W. Yin, "An iterative regularization method for total variation-based image restoration," *Multiscale Modeling & Simulation*, vol. 4, no. 2, pp. 460–489, 2005.

[26] X. Qu, "Compressed sensing MRI based on nonsubsampled contourlet transform," *2008 IEEE International Symposium on IT in Medicine and Education*, pp. 693–696, Dec. 2008. [Online]. Available: http://ieeexplore.ieee.org/lpdocs/epic03/wrapper.htm?arnumber=4743955

[27] Y. Yu, M. Hong, F. Liu, H. Wang, and S. Crozier, "Compressed sensing MRI using Singular Value Decomposition based sparsity basis." *Conference proceedings : ... Annual International Conference of the IEEE Engineering in Medicine and Biology*

Society. IEEE Engineering in Medicine and Biology Society. Annual Conference, vol. 2011, no. 1, pp. 5734–7, Jan. 2011. [Online]. Available: http://www.ncbi.nlm.nih.gov/pubmed/22255642

[28] K. Held, E. R. Kops, B. J. Krause, W. M. Wells III, R. Kikinis, and H.-W. Muller-Gartner, "Markov random field segmentation of brain mr images," *Medical Imaging, IEEE Transactions on*, vol. 16, no. 6, pp. 878–886, 1997.

[29] A. Blake, P. Kohli, and C. Rother, *Markov random fields for vision and image processing*. Mit Press, 2011.

[30] J. Lafferty, A. McCallum, and F. C. Pereira, "Conditional random fields: Probabilistic models for segmenting and labeling sequence data," 2001.

[31] A. Jordan, "On discriminative vs. generative classifiers: A comparison of logistic regression and naive bayes," 2002.

[32] V. Vapnik, *The nature of statistical learning theory*. Springer Science & Business Media, 2013.

[33] P. F. M. J. Shafiee, A. Wong, P. Siva, "Efficient Bayesian Inference using Fully Connected Conditional Random Fields with Stochastic Cliques," in *IEEE ICIP*, 204, p. 5.

[34] S. Ljunggren, "A simple graphical representation of fourier-based imaging methods," *Journal of Magnetic Resonance (1969)*, vol. 54, no. 2, pp. 338–343, 1983.

[35] C.-M. Tsai and D. G. Nishimura, "Reduced aliasing artifacts using variable-density k-space sampling trajectories," *Magnetic resonance in medicine*, vol. 43, no. 3, pp. 452–458, 2000.

[36] P. Gulaka and S.-c. Choi, "Method and apparatus for capturing magnetic resonance image," Nov. 4 2014, uS Patent 8,878,535.

[37] H. Nyquist, "Certain topics in telegraph transmission theory," *American Institute of Electrical Engineers, Transactions of the*, vol. 47, no. 2, pp. 617–644, 1928.

[38] Q. Huynh-Thu and M. Ghanbari, "Scope of validity of psnr in image/video quality assessment," *Electronics letters*, vol. 44, no. 13, pp. 800–801, 2008.

[39] E. Li, F. Khalvati, M. J. Shafiee, M. A. Haider, and A. Wong, "Sparse reconstruction of compressive sensing mri using cross-domain stochastically fully connected conditional random fields," *arXiv preprint arXiv:1512.07947*, 2015.

[40] F. Khalvati, A. Wong, and M. Haider, "Automated Prostate Cancer Detection via Comprehensive Multi-Parametric Magnetic Resonance Imaging Texture Feature Models," *Biomedical Central Medical Imaging*, vol. DOI 10.1186/s12880-015-0069-9, pp. 15–27, 2015.

[41] F. Khalvati, A. Modhafar, A. Cameron, A. Wong, and M. Haider, "A multi-parametric diffusion magnetic resonance imaging texture feature model for prostate cancer analysis," in *MICCAI 2014 Workshop on Computational Diffusion MRI*, 2014, pp. 79–88.

[42] A. Cameron, F. Khalvati, M. Haider, and A. Wong, "MAPS: A Quantitative Radiomics Approach for Prostate Cancer Detection," *IEEE Transactions on Biomedical Engineering*, vol. PP, pp. 1–12, 2015.

[43] A. Cameron, A. Modhafar, F. Khalvati, D. Lui, M. Shafiee, A. Wong, and M. A. Haider, "Multiparametric MRI Prostate Cancer Analysis via a Hybrid Morphological-Textural Model," in *International Conference of the IEEE Engineering in Medicine and Biology Society (EMBC)*, 2014, pp. 3357–3360.

[44] A. Chung, C. Scharfenberger, , F. Khalvati, A. Wong, and M. Haider, "Textural Distinctiveness in Multi-Parametric Prostate MRI for Suspicious Region Detection",," in *International Conference on Image Analysis and Recognition (ICIAR)*, 2015.

[45] J. Zhang, F. Khalvati, A. Wong, and M. Haider, "Superpixel-based Prostate Cancer Detection from Diffusion Magnetic Resonance Imaging," *Vision Letters*, vol. 1(1), p. VL107, 2015.

[46] A. Wong, F. Khalvati, and H. M. A, "Dual-Stage Correlated Diffusion Imaging," in *IEEE International Symposium on Biomedical Imaging (ISBI)*, 2015, pp. 75–78.

[47] F. Kazemzadeh, S. A. Haider, C. Scharfenberger, A. Wong, and D. A. Clausi, "Multispectral Stereoscopic Imaging Device : Simultaneous Multiview Imaging from the Visible to the Near-Infrared," *IEEE transactions on Instrumentation and Measurements*, vol. 63, no. 7, pp. 1871–1873, 2014.

[48] Z. Wang, A. C. Bovik, H. R. Sheikh, and E. P. Simoncelli, "Image quality assessment: from error visibility to structural similarity," *Image Processing, IEEE Transactions on*, vol. 13, no. 4, pp. 600–612, 2004.

[49] J. Lafferty and A. Mccallum, "Conditional Random Fields : Probabilistic Models for Segmenting and Labeling Sequence Data Conditional Random Fields : Probabilistic Models for Segmenting and," vol. 2001, no. Icml, pp. 282–289, 2001.

[50] K. A. Scott, E. Li, and A. Wong, "Sea Ice Surface Temperature Estimation Using MODIS and AMSR-E Data Within a Guided Variational Model Along the Labrador Coast," *IEEE Journal of Selected Topics in Applied Earth Observations and Remote Sensing*, pp. 1–1, 2014. [Online]. Available: http://ieeexplore.ieee.org/lpdocs/epic03/wrapper.htm?arnumber=6709797

[51] H. Park, Y. Dan, K. Seo, Y. J. Yu, P. K. Duane, M. Wober, and K. B. Crozier, "Filter-free image sensor pixels comprising silicon nanowires with selective color absorption." *Nano letters*, vol. 14, no. 4, pp. 1804–9, Apr. 2014. [Online]. Available: http://www.ncbi.nlm.nih.gov/pubmed/24588103

[52] H.-b. H. Care, D. Yi, C. Wang, H. Qi, L. Kong, F. Wang, and A. Adibi, "Real-Time Multispectral Imager for Home-Based Health Care," *IEEE Transactions on Biomedical Engineering*, vol. 58, no. 3, pp. 736–740, 2011.

[53] F. Kazemzadeh, M. J. Shafiee, A. Wong, and D. a. Clausi, "Reconstruction of compressive multispectral sensing data using a multilayered conditional random field approach," p. 921712, Sep. 2014. [Online]. Available: http://proceedings.spiedigitallibrary.org/proceeding.aspx?doi=10.1117/12.2062135

[54] A. Boroomand, A. Wong, E. Li, D. S. Cho, B. Ni, and K. Bizheva, "Multi-penalty conditional random field approach to super-resolved reconstruction of optical coherence tomography images." *Biomedical optics express*, vol. 4, no. 10, pp. 2032–50, Jan. 2013. [Online]. Available: http://www.pubmedcentral.nih.gov/articlerender.fcgi?artid=3799664&tool=pmcentrez&rendertype=abstract

[55] H. Park and K. B. Crozier, "Multispectral imaging with vertical silicon nanowires." *Scientific reports*, vol. 3, p. 2460, Jan. 2013. [Online]. Available: http://www.pubmedcentral.nih.gov/articlerender.fcgi?artid=3746203&tool=pmcentrez&rendertype=abstract

[56] K. Hirakawa and T. W. Parks, "Adaptive homogeneity-directed demosaicing algorithm," *Image Processing, IEEE Transactions on*, vol. 14, no. 3, pp. 360–369, 2005.

[57] D. Alleysson, S. Süsstrunk, and J. Hérault, "Linear demosaicing inspired by the human visual system," *Image Processing, IEEE Transactions on*, vol. 14, no. 4, pp. 439–449, 2005.

[58] H. S. Malvar, L.-w. He, and R. Cutler, "High-quality linear interpolation for demosaicing of bayer-patterned color images," in *Acoustics, Speech, and Signal Processing,*

2004. Proceedings.(ICASSP'04). IEEE International Conference on, vol. 3. IEEE, 2004, pp. iii–485.

[59] R. Kimmel, "Demosaicing: image reconstruction from color ccd samples," *Image Processing, IEEE Transactions on*, vol. 8, no. 9, pp. 1221–1228, 1999.

[60] S. Farsiu, M. Elad, and P. Milanfar, "Multiframe demosaicing and super-resolution of color images," *Image Processing, IEEE Transactions on*, vol. 15, no. 1, pp. 141–159, 2006.

[61] X. Li, "Demosaicing by successive approximation," *Image Processing, IEEE Transactions on*, vol. 14, no. 3, pp. 370–379, 2005.

[62] X. Li, B. Gunturk, and L. Zhang, "Image demosaicing: A systematic survey," in *Electronic Imaging 2008*. International Society for Optics and Photonics, 2008, pp. 68 221J–68 221J.

[63] K.-H. Chung and Y.-H. Chan, "Color demosaicing using variance of color differences," *Image Processing, IEEE Transactions on*, vol. 15, no. 10, pp. 2944–2955, 2006.

[64] M. F. Tappen, B. C. Russell, and W. T. Freeman, "Exploiting the sparse derivative prior for super-resolution and image demosaicing," in *In IEEE Workshop on Statistical and Computational Theories of Vision*. Citeseer, 2003.

[65] H. R. Morris, C. C. Hoyt, and P. J. Treado, "Imaging spectrometers for fluorescence and raman microscopy: acousto-optic and liquid crystal tunable filters," *Applied spectroscopy*, vol. 48, no. 7, pp. 857–866, 1994.

[66] J. Y. Hardeberg, F. Schmitt, and H. Brettel, "Multispectral color image capture using a liquid crystal tunable filter," *Optical engineering*, vol. 41, no. 10, pp. 2532–2548, 2002.

[67] D. N. Stratis, K. L. Eland, J. C. Carter, S. J. Tomlinson, and S. M. Angel, "Comparison of acousto-optic and liquid crystal tunable filters for laser-induced breakdown spectroscopy," *Applied spectroscopy*, vol. 55, no. 8, pp. 999–1004, 2001.

[68] J. Brauers, N. Schulte, and T. Aach, "Multispectral filter-wheel cameras: Geometric distortion model and compensation algorithms," *Image Processing, IEEE Transactions on*, vol. 17, no. 12, pp. 2368–2380, 2008.

[69] A. K. Dunn, A. Devor, H. Bolay, M. L. Andermann, M. A. Moskowitz, A. M. Dale, and D. A. Boas, "Simultaneous imaging of total cerebral hemoglobin concentration, oxygenation, and blood flow during functional activation," *Optics letters*, vol. 28, no. 1, pp. 28–30, 2003.

[70] F. K. A. W. Edward Li, Mohammad Javad Shafiee, "Sparse reconstruction of compressed sensing multi-spectral data using cross-spectral multi-layered conditional random field model," S. Optics and Photonics, Eds., SPIE Optics and Photonics. SPIE Optics and Photonics, 2015.

[71] H. Park and K. B. Crozier, "Multispectral imaging with vertical silicon nanowires," *Scientific reports*, vol. 3, 2013.

[72] H. Park, Y. Dan, K. Seo, Y. J. Yu, P. K. Duane, M. Wober, and K. B. Crozier, "Filter-free image sensor pixels comprising silicon nanowires with selective color absorption," *Nano letters*, vol. 14, no. 4, pp. 1804–1809, 2014.

[73] V. Surya Prasath, D. Vorotnikov, R. Pelapur, S. Jose, G. Seetharaman, and K. Palaniappan, "Multiscale tikhonov-total variation image restoration using spatially varying edge coherence exponent," *Image Processing, IEEE Transactions on*, vol. 24, no. 12, pp. 5220–5235, Dec 2015.

[74] X. Wang and L. Zhang, "Compressed sensing image reconstruction algorithm based on regional segmentation," in *Image and Signal Processing (CISP), 2014 7th International Congress on*, Oct 2014, pp. 207–211.

[75] S. Li, X. Tao, Y. Li, and J. Lu, "Large-scale structured sparse image reconstruction with correlated multiple-measurement vectors using bayesian learning," in *Picture Coding Symposium (PCS), 2015*, May 2015, pp. 272–276.

[76] P. Erds and R. Alfréd, "On Random Graphs I," *Publ. Math. Debrecen*, vol. 6, pp. 290–297., 1959.

[77] W. K. Hastings, "Monte Carlo sampling methods using Markov chains and their applications," *Biometrika*, vol. 57, no. 1, pp. 97–109, 1970. [Online]. Available: http://biomet.oxfordjournals.org/content/57/1/97.short

[78] T. Esen, B. Turkbey, A. Patel, and J. Futterer, "Multiparametric mri in prostate cancer," *BioMed Research International*, 2014.

[79] D. Cho, F. Khalvati, A. Wong, and M. A. Haider, "Prostate DWI Co-Registration via Maximization of Hybrid Statistical Likelihood and Cross-Correlation for Improved ADC and Computed Ultra-High b-value DWI Calculation," in *International Society for Magnetic Resonance in Medicine (ISMRM)*, 2015, p. 3748.